Understanding Bipolar Membrane Durability and Performance in High-Current Electrochemical Systems

by

Olivia T. Vulpin

A dissertation accepted and approved in partial fulfillment of the

requirements for the degree of

Doctor of Philosophy

in Chemistry

Dissertation Committee:

Dave Johnson, Chair

Shannon Boettcher, Advisor

Paul Kempler, Core Member

Roman Alvarado, Institutional Representative

University of Oregon

Spring 2025

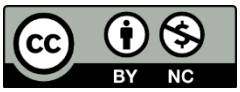

DISSERTATION ABSTRACT

Olivia T. Vulpin

Doctor of Philosophy in Chemistry

Title: Understanding Bipolar Membrane Durability and Performance in High-Current Electrochemical Systems

With the growing demand for climate technology as the predicted effects of climate change become reality, researchers have been turning to electrochemical stack systems. These systems provide a way to transition from utilizing fossil fuels to electricity, while also providing novels means of chemical production, CO_2 sequestration, and fuel generation. A major pain point for electrochemical stack researchers is the high resistance of the bipolar membrane (BPM) found in a range of these stack systems. The BPM is made of two ion-exchange polymers sandwiched together, and when an electric field is established across the BPM, water is split into protons and hydroxide ions. The BPM is thus a simple way to introduce pH change through electricity, instead of relying on the introduction of chemicals, which are potentially polluting and require complex setups. However, the energy required to split water is relatively high, and thus the driver of BPM resistance, slowing the adoption of this technology. To address the higher overpotential required to split water in the BPM, the Boettcher lab has been working to introduce water dissociation catalysts to the BPM, with much success. The introduced catalyst was proven in fundamental electrochemical stacks, and here we explore expanding the use case for these catalyzed BPMs. For this, an electrochemical test platform was developed to analyze and record the potential drops across each component of the electrochemical stack. This system also monitor how the introduced catalysts withstood the introduction of potentially fouling environments. It was found that with the introduction of the catalyzed BPM, there was a two-fold reduction in energy consumption compared to incumbent BPMs in the same system, and the catalyzed BPM presented acceptable durability at high currents. Furthermore, the catalyzed BPM was able to maintain current efficiency of ~90% from 0.05-0.5 A cm^{-2}, with improved current efficiency as the current was increased. Additionally, with the introduction of new BPM manufacturing techniques, a 600x improvement in BPM layer adhesion was found at no cost to BPM performance. These developments allow the BPM to be implemented in a wide range of existing electrochemical stacks with little re-engineering required.

This dissertation includes previously published material in Chapter III, Vulpin et al. *ACS Energy Letters* **2025**, and unpublished material in Chapter IV, which has the co-authors: Ben Indeglia, James B. Mitchel, Sayantan Sasmal, Karen Winey & Shannon W. Boettcher.

CURRICULUM VITAE

NAME OF AUTHOR: Olivia T. Vulpin

GRADUATE AND UNDERGRADUATE SCHOOLS ATTENDED:

University of Oregon, Eugene, Oregon, United States of America
Eckerd College, St. Petersburg, Florida, United States of America

DEGREES AWARDED:

Doctor of Philosophy, Chemistry, 2025, University of Oregon
Bachelor of Science, Marine Science, 2019 Eckerd College
Bachelor of Science, Chemistry, 2019 Eckerd College

AREAS OF SPECIAL INTEREST:

Electrochemistry: Electrochemical Stack Devices; Bipolar Membranes
Climate Technology: Direct Air Capture Systems; CO_2 Electrolyzers; Electrodialysis
Systems Development and Manufacturing: CNC Machining; CAD

PROFESSIONAL EXPERIENCE:

Graduate Employee, University of Oregon, 2020-2025
Pursuing Ph.D. under Dr. Shannon Boettcher

Biogeochemical Analyst, University of South Florida, 2018-2020
Research Assistant under Dr. Isabel Romero

Lab Analyst, Benchmark EnviroAnalytical, 2016-2018

PUBLICATIONS:

Vulpin, O. T.; Mitchell, J. B.; Chen, L.; Lim, J.; Sasmal, S.; Price, N. G.; Jarvis, S. R.; Boettcher, S. W. Comparing Advanced Bipolar Membranes for High-Current

Electrodialysis and Membrane Electrolysis. *ACS Energy Lett.* **2025**, 845-852. DOI: 10.1021/acsenergylett.4c03538.

Han, S.; Sasmal, S.; Shen, M.; Wu, Y.; **Vulpin, O. T.**; Hou, S.; Kim, S.; Lee, J. Y.; Yoon, J.; Boettcher, S. W. Advancing SnO2-Based Water Dissociation Catalysis in Bipolar-Membrane Water Electrolyzers. *ACS Energy Lett.* **2025**, 1633-1641. DOI: 10.1021/acsenergylett.5c00309.

Sasmal, S., Chen, L., Sarma, P.V., **Vulpin, O.T.**, Simons, C.R., Wells, K.M., Spontak, R.J., & Boettcher, S.W. (2024). Materials descriptors for advanced water dissociation catalysts in bipolar membranes. *Nature materials*.

Ahn, S. M.; Boudreau, A.; Ekennia, A. C.; Palau, A.; **Vulpin, O. T.**; Kwak, M.; Kim, Y. S.; Boettcher, S. W.; Park, E. J.; Roberts, G. M.; et al. Anion exchange membrane test protocol validation. *Front. Energy Res.* **2025**, *13*, Methods. DOI: 10.3389/fenrg.2025.1553134.

TABLE OF CONTENTS

LIST OF FIGURES

Figure Page

LIST OF TABLES

Table Page

CHAPTER I

INTRODUCTION

Globally, we are experiencing the full force of climate change. With rises in global temperatures, water scarcity has become a reality for 47% of the world's population, and this is predicted to rise to 53% by 2050.[1] This warming stems from the increase in greenhouse gases found in the atmosphere. These gases act as a blanket over the earth, preventing heat from naturally emitting out to space and instead trapping it within the atmosphere. This has inspired many to call for significant reductions in greenhouse gas emissions and for removing greenhouse gases from the atmosphere to help reduce the warming of our planet.[2] These greenhouse gases consist of a cocktail of radiation-absorbing molecules, with CO_2 making up the majority and gases like nitrous oxide and methane making up a smaller, but important, percentage. Researchers have been working to address the issues resulting from climate change. Three major efforts in the fight against climate change are: reducing reliance on fossil fuels for various processes, removing CO_2 emitting steps from industrial processes, and increasing water recycling and purification.

The most significant change is to reduce or eliminate our reliance on fossil fuels. To meet this goal, the electrification of industrial processes has made great strides. This electrification allows for a transition from fossil fuel burning power plants to renewable energy sources, like wind and solar. One of the keys to electrification is the introduction of electrochemistry. Electrochemistry is, basically, the utilization of electricity to either oxidize or reduce a species in solution. With this simple, but powerful, tool, chemistry can be performed without the need for petroleum-based chemicals that are inherently reliant on fossil fuels. This transition is known as "green chemistry" and has been adopted by a range of different chemical producing industries. Electrochemistry can also be used to reduce industrial reliance on high-temperature furnaces. The generation of heat alone accounts for approximately 21% of the annual CO_2 emissions from the industrial sector.[3] Electrochemistry can be used to produce hydrogen, utilizing an electrolyzer stack, which can be used to reduce iron oxide in the steel making process. This process was previously performed using high heat and carbon monoxide, which inherently emits CO_2 as a by-product.

In the same vein as using an alternative method to introduce reduction to the steel making process, cement production can also be reimagined. Cement production itself accounts for approximately 8% of global CO_2 emissions due to the inherent CO_2 emission step in the cement clinker production process.[4, 5] Utilizing electrochemistry, this clinker production step can be done in a controlled manner at low temperatures that allow for easy sequestration of the CO_2 emitted from this process (Figure 1.1a).

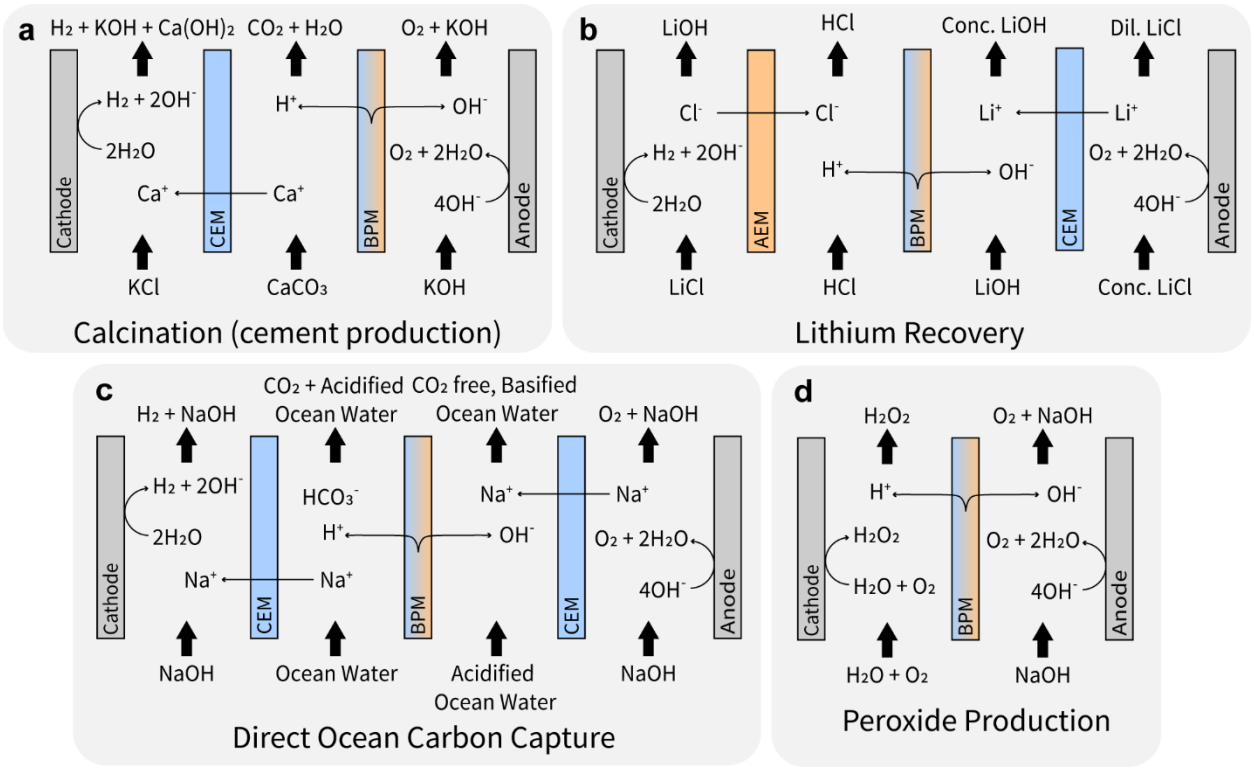

Figure 1.1: Example electrochemical stack schematics showing the wide range of uses for ion-exchange membranes and stack configurations. With examples of cement production through a contained CO_2 calcination step (a), lithium recovery from lithium salts into a usable lithium hydroxide form (b), carbon capture from ocean water (d), and peroxide production that does not require harsh chemicals (d).

This same method can then be adopted for use in the extraction of CO_2 from natural sinks, like the ocean or atmosphere, allowing for a more permanent sequestration of this captured carbon and a return to the natural carbon cycle (Figure 1.2). This sequestration can be done using electrochemical stacks like those seen in Figure 1.1c, where sea water is input into the system and CO_2 free, basified sea-water is returned to the ocean. This basification not only helps with countering the acidification effect due to increased CO_2 by the ocean, it also allows the ocean to sequester additional CO_2.

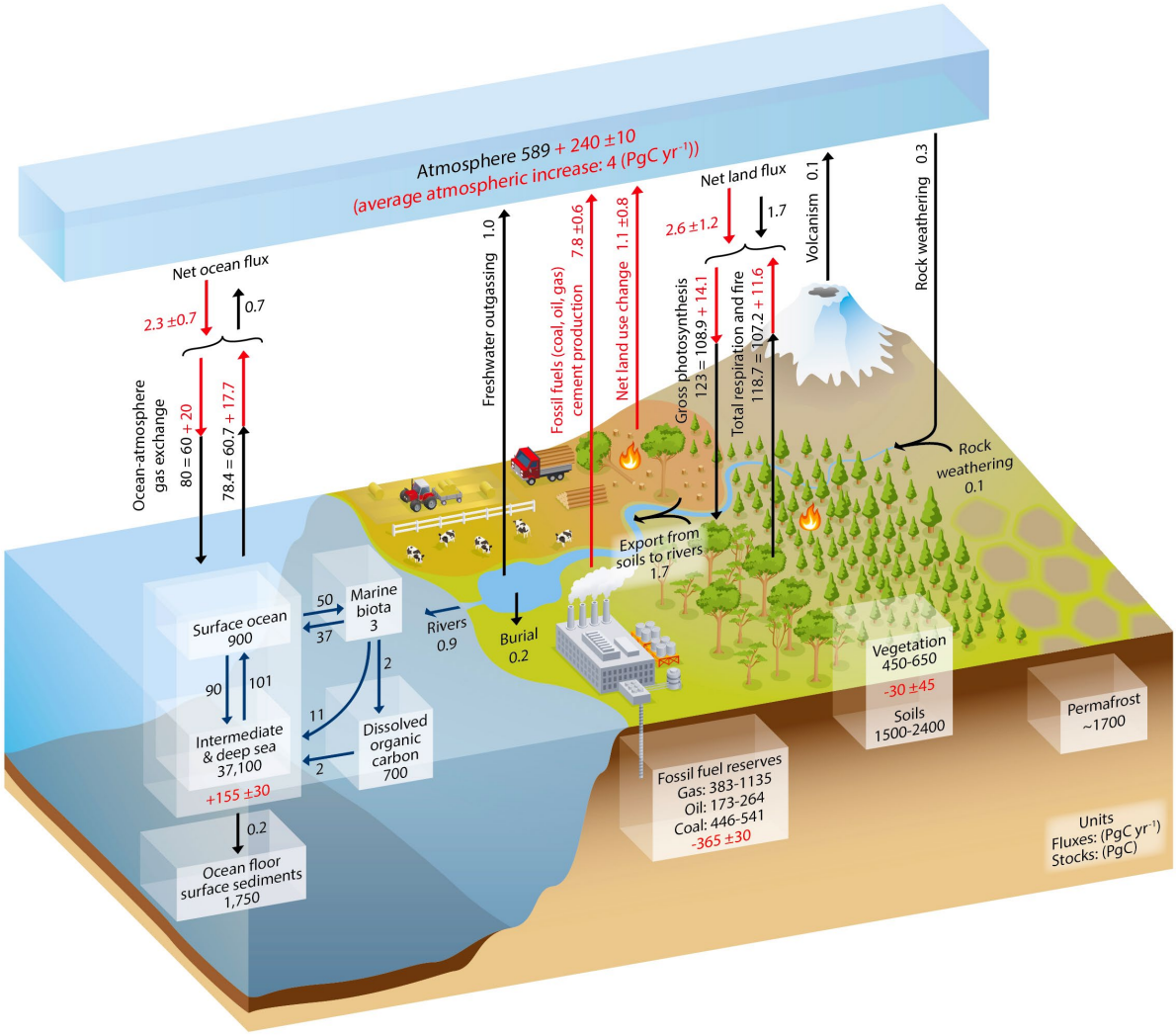

Figure 1.2: Schematic showing the cycle of carbon and the depletion of natural carbon sinks and the dispersion of carbon into the atmospheres and oceans. This figure was obtained from IPCC, 2013: Climate Change 2013: The Physical Science Basis. Contribution of Working Group I to the Fifth Assessment Report of the Intergovernmental Panel on Climate Change.[6]

While the removal of CO_2 helps address the root cause of climate change, these systems do not address the felt effects of climate change today. One of the key issues plaguing communities is water scarcity and polluted groundwater. Electrochemical stacks can also be used to further process industrial brine waste, not only extracting the water out, but reducing the likelihood this waste will leach into groundwater and lead to pollution. These systems also incentivize industries to reduce their liquid brine waste by introducing the valorization of this waste. With these electrochemical stacks, the waste not only has the water removed and recycled, but it also produces

value adding acid and base. These acid and base products can be sold, or reused in the industrial process.

While electrochemical systems seem to provide a variety of solutions to climate change, few of these systems are seen, even at the pilot scale. There are still key fundamental issues that prevent the adoption of these systems. To move us toward addressing these key pain points, I have focused on addressing the key issue associated with bipolar membranes (BPM). This membrane is found in a wide range of these electrochemical stacks, and is often the point of highest resistance, leading to the systems being energy inefficient. A BPM is comprised of two layers of polymer that utilize an electric field to split water into H^+ and OH^-, allowing for the acidification and basification of adjacent flowing solutions. The issue with these membranes stems from the energy required to split water. To address this issue, the Boettcher lab has been working to introduce water dissociation catalysts to BPMs, making significant breakthroughs and reducing the energy requirement to near the thermodynamic limit.[7] However, these advancements were made in an idealized system, and to better understand how these ground breaking catalysts would function in a wider range of electrochemical stacks, I began development of a lab scale test platform that could be used to assess the durability of the catalyst in systems that contained potentially fouling co-ions, and presented different mechanical stressors on the BPM. The test platform is discussed in Chapter II, and the expanded use case of the catalyzed BPM is discussed in Chapter III, where it was published as Vulpin et al. *ACS Energy Letters* **2025**. With these applications, more questions and issues arose, and in Chapter IV the delamination and blistering of the BPM layers are discussed and addressed, this data is unpublished as the co-authors include: Ben Indeglia, James B. Mitchel, Sayantan Sasmal, Karen Winey & Shannon W. Boettcher.

Overall, we show cased the expanded application of catalyzed BPM to electrochemical systems like BPM electrodialysis. In the BPM electrodialysis system, the overpotential for water dissociation was only 0.2 V higher at 0.5 A cm^{-2} compared to the values seen in the idealized electrochemical stack. Additionally, the catalyzed BPMs were able to maintain a current efficiency of ~90% from 0.05-0.5 A cm^{-2}, showed a voltage loss of only ~0.31 mV h^{-1} over 80 hours, and showed a two-fold decrease in energy consumption compared to incumbent BPMs. To address durability and mechanical issues, different methods to increase adhesion between the two layers making up the BPM were explored. It was found that the electrostatic attraction between the two BPM layers worked well to hold the layers together. Unfortunately, when a catalyst layer

was introduced, these attractions were interrupted and alternate means of adhesion had to be introduced to the BPM. To introduce adhesion, solvent was used to swell the backbone of one of the layers, while the other layer was introduced as a cast polymer solution. The mobility of the polymers in the cast solutions allowed for the migration of the polymer backbones into the adjacent swollen membrane, forming a physical interlock when the solvent was baked off. This lead to BPMs that were not only catalyzed, but also showed a two orders of magnitude improvement in layer adhesion.

CHAPTER II

DESIGNING A LABSCALE ELECTRODIALYSIS TEST PLATFORM

Introduction

While established electrodialysis systems exist at the small scale, these systems are still too large for reasonable lab testing and do not provide enough resolution of the system itself to be useful for fundamental research on the function of bipolar membranes (BPM) in electrochemical stack systems. Typically, labs use a system produced by PCCell, which has an active area of 8x8 cm^2, requiring fairly large membranes. Alternatively, electrolyzer test systems, like those from Fuel Cell Store, require a membrane active area of only 1x1 cm^2. With smaller active areas, labs can spend less money on the membrane materials themselves, and do not have to develop scaled membranes, saving not only money, but labor time. Furthermore, systems like PCCell allow for only rudimentary analysis of the electrochemical system, thus making it difficult to deconvolute the "black box" of electrochemical stacks.

To address the issues found with the commercially available lab-scale electrodialysis system, I ventured to construct my own system. The main goal for the system was to design something that can use small active area membranes (1x1 cm^2), modular enough to test a wide range of different electrochemical stack systems, and introduce monitoring strategies to allow for a more complete understanding of the components within the electrochemical stack.

System description

The BPMED systemhas two major sections; the BPMED stack and the test stand (Figure 2.1). These sections are required for running electrochemical protocols and collecting electrochemical data. The system's DIY nature encourages labs to assemble the test stand and stack to suit their needs, and here the example of a BPMED configuration is used.

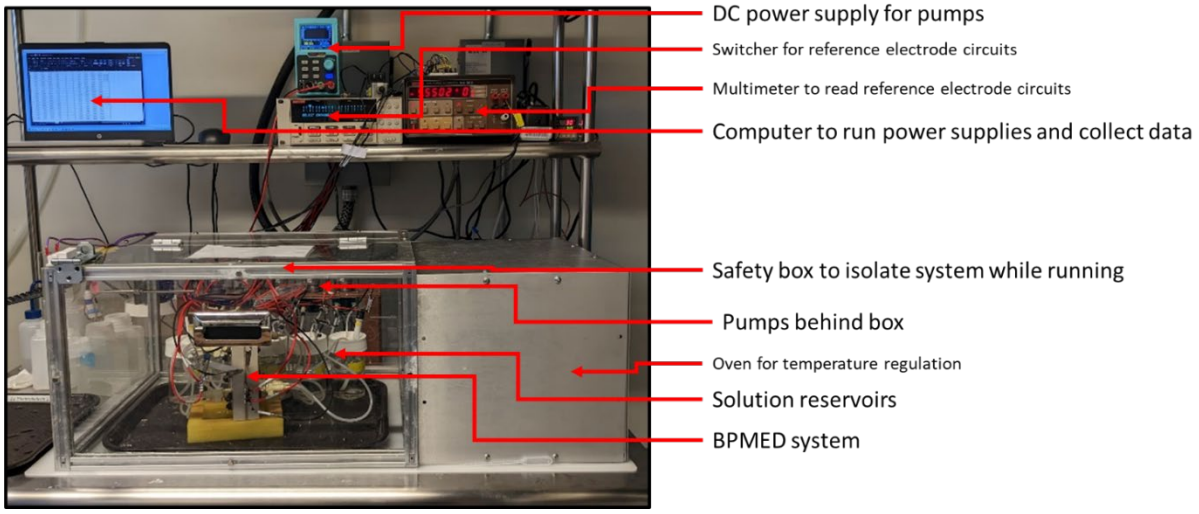

Figure 2.1: Example BPMED test stand and stack.

BPMED stack.

The initial construction of the stack required cutting PTFE gaskets and machining the stack endplates and flow fields (Figure 2.2). All the internal gaskets of the BPMED stack are made with varying thicknesses of PTFE film cut using a vinyl cutter.

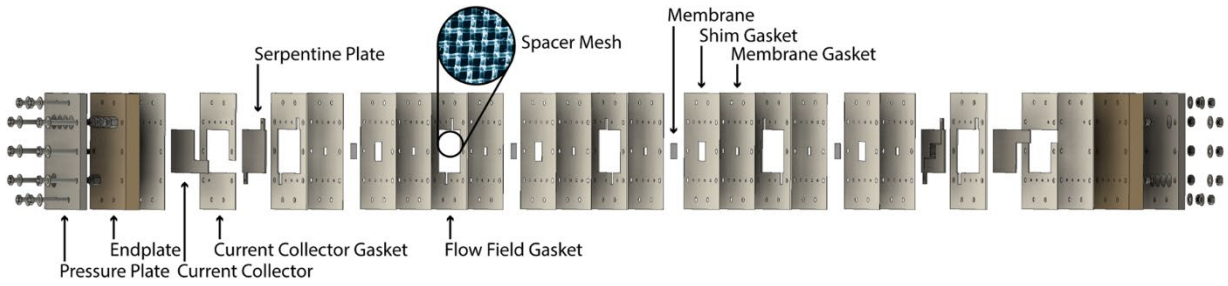

Figure 2.2: Exploded schematic of BPMED stack.

The thickness of each gasket section was tailored to perfectly fit the component that fills those sections of gasket. For example, the spacer mesh used for the BPMED system is 0.006" thick, thus requiring gasketing that has a total thickness of 0.006". For areas where the thickness of the component is larger than 0.01", the compression of the PTFE may require troubleshooting of the gasket thickness. For troubleshooting, SPI pressure paper was used to ensure that the component inside the gasket was as flush as possible with the gasket for that component. The goal was to

prevent leakage around the gaskets and to ensure a good seal around the different components of the BPMED system.

The endplates, pressure plates, and serpentine plates must be machined. The endplate material is ideally a non-conductive, rigid material. Thus, PEEK or Delrin are good candidates, especially given the ease of machining these plastics. The pressure plates must be within a tight tolerance and rigid, thus cold ground aluminum or steel works well. The pressure plates can be cut using a water jet to avoid expensive CNC mill time. The most expensive part of the BPMED stack is the serpentine plates. The serpentine plates have extremely small channels to ensure good bubble evacuation and are ideally corrosion resistant, requiring a material such as 316 stainless steel. Given the requirements for small features on a hard material, a skilled machine shop is required for adequate manufacturing of this component.

The last major component of the BPMED stack are the current collectors. The material for the current collectors must be conductive and corrosion resistant, thus 316 stainless steel is a good choice. To cut the thin stainless steel sheets, a fiber laser was utilized.

With all the BPMED stack components constructed, the assembly of the BPMED stack begins at the cathode side. By carefully threading the gaskets onto the bolts (here used as locating dowels) each component can be placed inside its gasket. Through this process the system is assembled layer by layer. Once the full system is assembled appropriately, the anode endplate and pressure plate are placed on top. Washes and nuts are threaded on the ends of the bolts and hand tightened before sequentially torqued to 25 in-lbs, then 50 in-lbs, and finally 85 in-lbs, while following a star-pattern. The stack is now ready to be hooked up to the test stand.

Test stand.

For the test stand, a computer equipped with LabView software is required to operate the different components of the test stand and to record the data while executing procedures. The test stand itself will include a switcher, a multimeter, an enclosed oven, at least five peristaltic pumps, and a power supply. All of these different components are ideally controlled by a LabView program, using GPIB connections or USB connections. For the switcher, there are a total of eight channels that need to be controlled and fed into the multimeter.

The stack is placed within a temperature controlled oven where the solution reservoirs are kept at the same temperature as the overall stack itself. Temperature can have a large impact on

the kinetics of various reactions in the BPMED system and should be controlled.[8] The stack should be oriented with the inlets on the bottom of the system and the outlets on the top, allowing for the most efficient bubble evacuation from the BPMED stack. Further details on bubble issues can be found below. Each reservoir will have its own reference electrodes, ideally electrodes that are stable in the pH of the reservoir solutions (Figure 2.3).

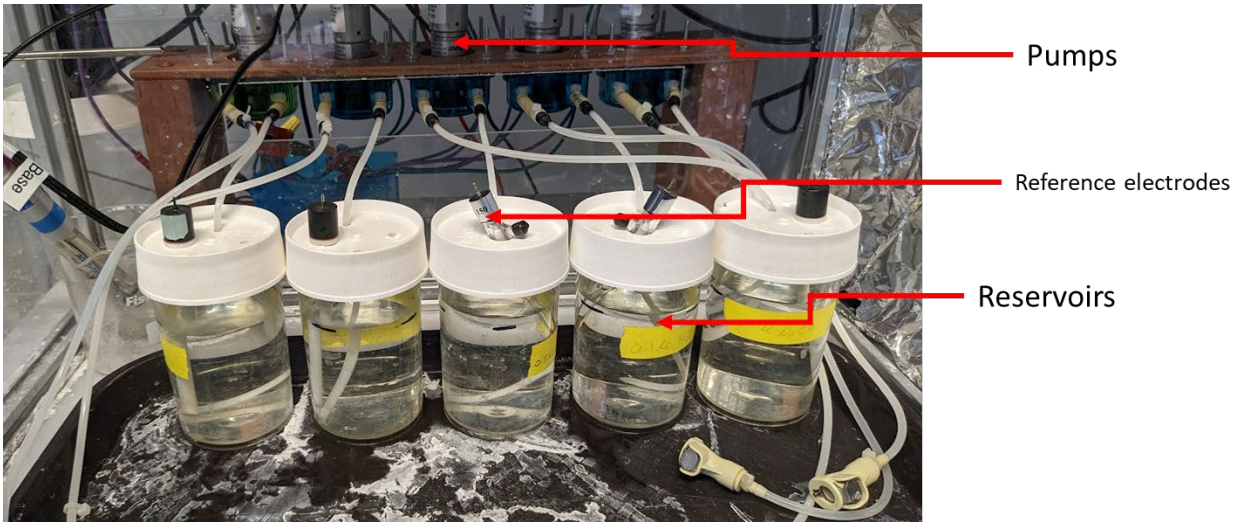

Figure 2.3: Example of five solution reservoirs with associated peristaltic pumps and reference electrodes.

For example, standard calomel electrodes (SCE) are used for acid solutions, and mercury/mercury oxide electrodes (Hg/HgO) are used in basic solutions.

The switcher is designed to step through each of these channels channel, recording the components of the overall electrochemical stack (Figure 2.4).

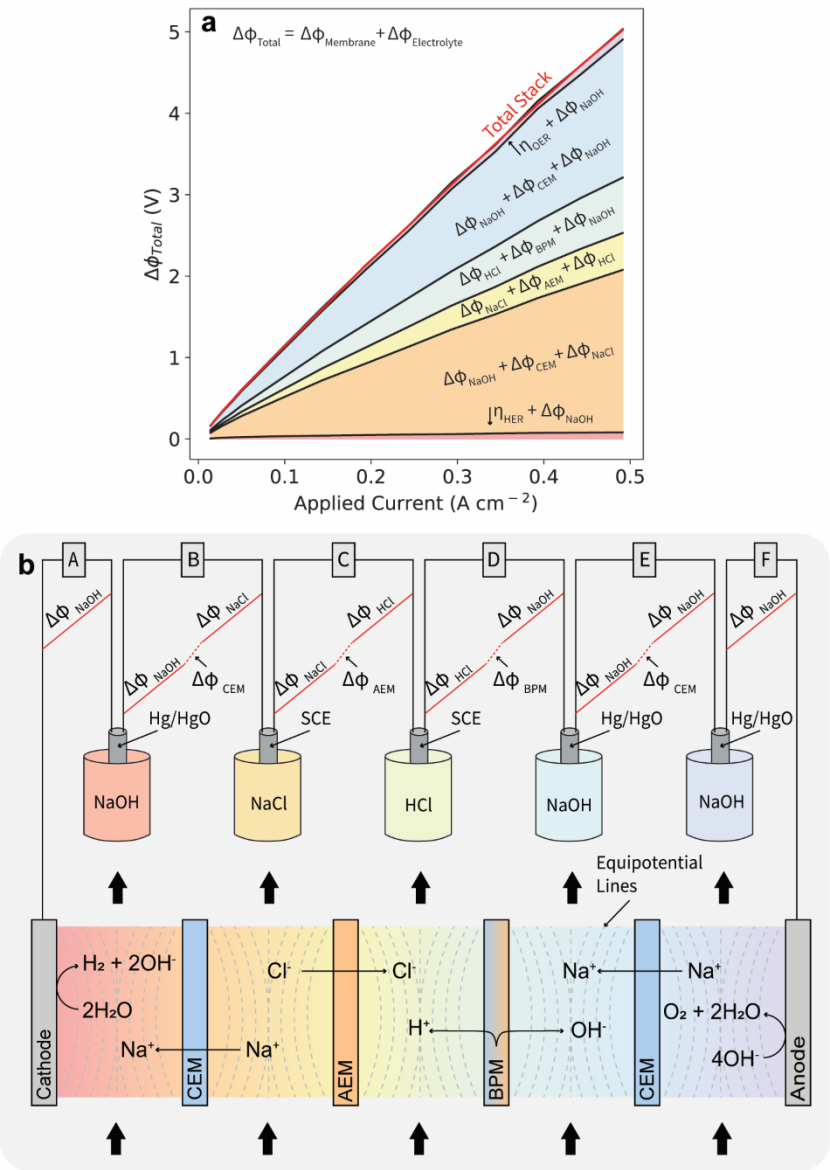

Figure 2.4: (a) Overpotential across each measured circuit throughout the BPM electrodialysis system (i.e. potential change as a function of current, relative to the open-circuit value), totaling to the measured entire system voltage (total stack) at 25 °C. **(b)** Schematic of the membrane and electrolyte layers in the BPM electrodialysis stack, with the different measured potential drop circuits labeled **A** through **F** and schematic potential drops ($\Delta\phi$) within each circuit. The $\Delta\phi$ moving from the center from one flow channel, across a membrane, and to the center of an adjacent flow channel are measured using reference electrodes in the reservoirs feeding each electrolyte flow of the overall stack. The color gradients schematically represent the potential gradients in each section of the electrodialysis stack. We take each reservoir (represented as the uniform-colored cylinders) as equipotential to the electrolyte at approximately the midpoint of the flow channel represented by the vertical dashed line. An ohmic potential drop is present across the electrolyte region and the membrane region of the system. The measured steady-state voltage changes also include contributions from concentration polarization in addition to contributions from electric-potential drops driving migration. Circuits **A** and **F** further include the reaction kinetic overpotentials which are not important in this study but contribute to the overall cell voltage.

The system's channels include channels across the anode and cathode, recording the potential drop for the half reactions in the stack, then channels for each of the membranes within the total stack. Additional useful channels include a channel that records the total stack potential, from anode to cathode, and a channel across a 1 Ω resistor, that can be used to record the current going through the stack itself (Figure 2.5).

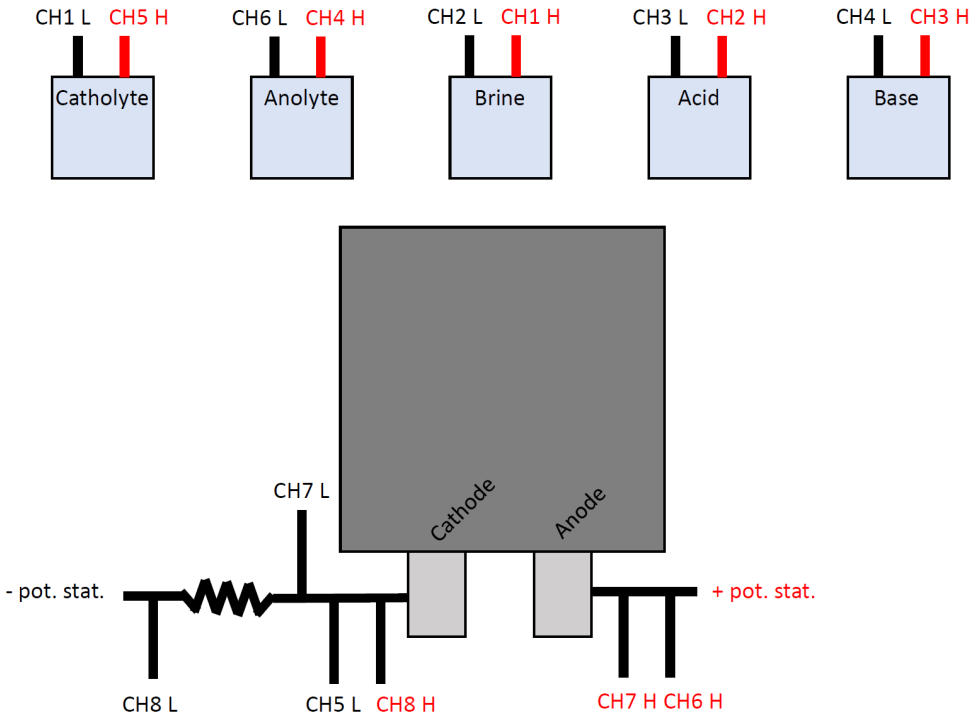

Figure 2.5: Basic wiring diagram for the full BPMED system test stand. Blue squares represent reservoir solutions with wires attached to reference electrodes in these solutions. The grey box represents the assembled BPMED stack in the test stand, with protruding current collectors.

Each step of the multimeter includes a programmed step that opens all the channels, followed by a step that closes the next desired channel to be recorded. These steps can occur quickly in sequence to prevent dramatic fluctuations in the recording. The switcher output leads are wired to the input leads on the multimeter, so that when the switcher channel is closed, the multimeter will be reading the potential of that specific channel. Using the multimeter, the potential for the channel is recorded by the computer, using a recording step in LabView. Once the channel has been closed, then recorded by the computer through the multimeter, the channels

are all opened, and the next channel is closed, and so on. Once all the channels have been recorded, the power supply is prompted to the next potential, or current, in its stepping routine.

System operation

General.

Before the assembled system is connected to the test stand, the pumps and tubing should be primed with fresh solution. For this, fill all the reservoirs with the desired solutions, connect the inlet tubing to an unassembled endplate, and flow electrolyte through the pumps and tubing for ~7-10 seconds (Figure 2.6).

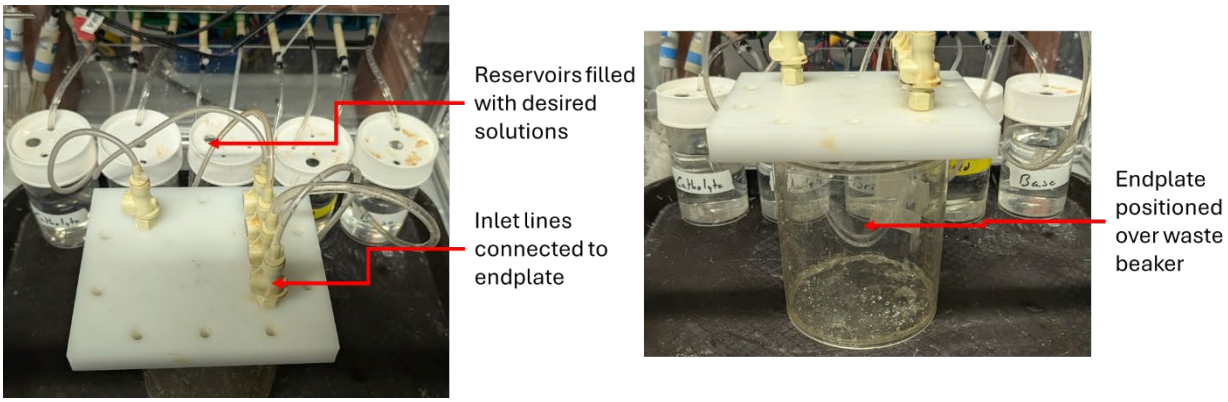

Figure 2.6: Images depicting the initial pump/tubing rinse step.

With the pumps primed, the inlet and outlet tubing can be connected to the assembled electrodialysis system. First connect the anode side, while the system is laying on the assembly stand, then turn the system upright to connect the cathode side tubing. Be sure to have the inlet tubing at the bottom of the system and the outlet tubing at the top (Figure 2.7).

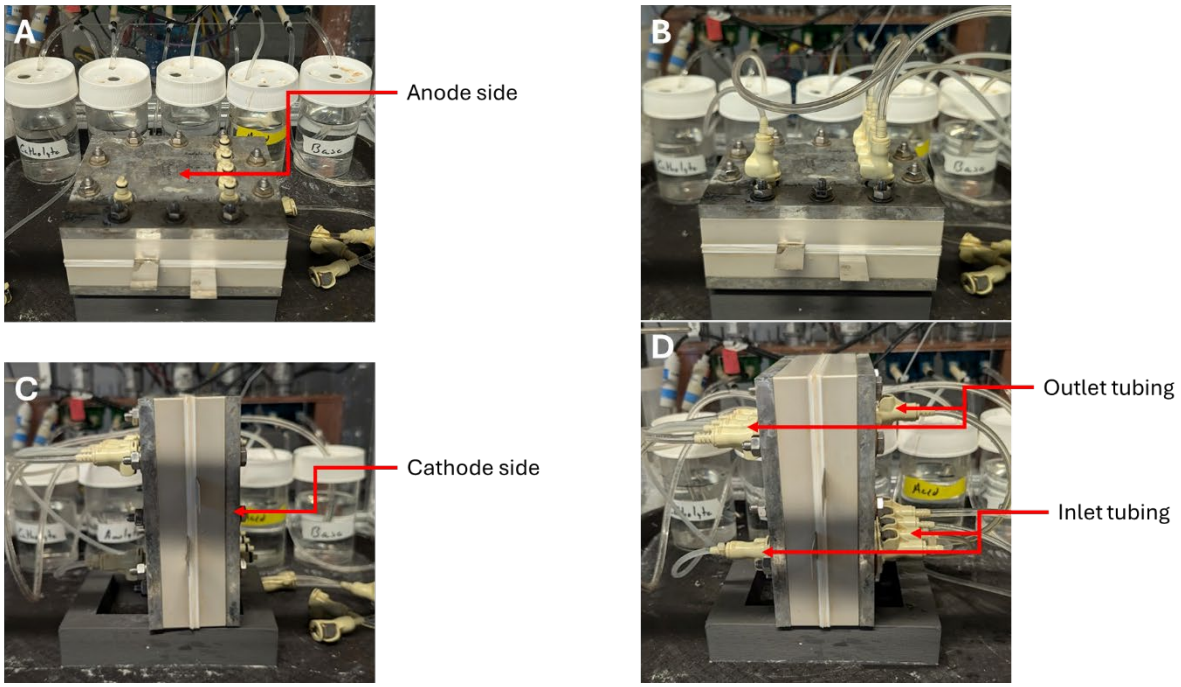

Figure 2.7: Labeled image showing the steps (A-D) of attaching the solution tubing to the assembled electrodialysis system.

The orientation of the BPMED stack is to ensure proper bubble evacuation from the electrolyte flow fields. Then connect the appropriate tubing to each respective reservoir.

Polarization Curve Protocol.

Polarization curves allow for the generation of current versus voltage plots (Figure 2.4a). For polarization-curve data, the initial catholyte and anolyte streams were 1.0 M NaOH, the brine stream was 1.0 M NaCl, the acid stream was 1.0 M HCl, and the base stream was 1.0 M NaOH. Current steps were made in increments of 10 mA cm^2 from 0-50 mA cm^2, then increments of 50 mA cm^2 were made from 100-500 mA cm^2. Each current step was held for 10 seconds, and each circuit (A-F) was measured twice (Figure 2.4b). The currents were stepped up and down once, with the data being analyzed from the downward ramp to assure consistent conditions of the membranes in the stack. Before the power supply was turned on, the open circuit potentials (OCV) were recorded for each circuit, and these were again recorded after the current was ramped up, then down.

Current Efficiency Protocol.

Current efficiency data allows one to assess the current utilization of the BPMED system. The current utilization allows for insight into a BPM's acid and base production, and will reveal potential ion leakage issues in the membrane or the BPMED system. For current-efficiency data collection, the stack was assembled with the desired BPM, and alternate solutions were used in the BPMED system to best compare results to literature and to reduce error during titration. The catholyte and anolyte solutions were kept as 1.0 M NaOH, the brine solution was increased to 3.0 M NaCl, and both the acid and base solutions were initially 0.50 M NaCl. For each tested BPM, current was first held at 100 mA cm^{-2} for 30 min to exchange the membrane and condition the system. Once this conditioning was complete, the solutions in each reservoir were replaced. The pumps were run for 30 seconds to mix any remaining acid and base that may be either in the stack or in the system's tubing. Once well mixed, the initial titration sample was extracted from the reservoir, and current was applied to the stack. After 30 minutes, the current and the pumps were stopped, the volume of the reservoir was recorded, and the final titration sample was extracted. This process was repeated for each current step (50, 100, 250, 500, then ending with another 50 mA cm^{-2}).

With all the samples collected from the five different runs, the acid and base samples are titrated to best determine their proton or hydroxide ion concentrations. Prior to titration, the auto-titrator pH probes were calibrated before every run, 0.10 M KOH titrant was calibrated using potassium hydrogen phthalate (KHP), and a 0.10 M HCl solution was calibrated using the titrator. Titration samples were prepared by weight, as described in Table 2.1.

Table 2.1: Sample preparation for titration.

Run Number	Current Applied (A cm^{-2})	Initial Sample		Final Sample	
		Sample Weight	0.10 M HCl added	Sample Weight	0.10 M HCl added
Run 1 – Acid	50	20	1	20	0
Run 2 – Acid	100	20	1	10	0
Run 3 – Acid	250	20	1	5.5	0
Run 4 – Acid	500	20	1	2.5	0
Run 5 – Acid	50	20	1	20	0
Run 1 – Base	50	20	1	20	2
Run 2 – Base	100	20	1	10	2
Run 3 – Base	250	20	1	5.5	2
Run 4 – Base	500	20	1	2.5	2
Run 5 – Base	50	20	1	20	2

The calibrated 0.10 M HCl was added to the initial samples, as these samples would have little to no acid and base present but may vary slightly due to the mixing step between reservoir solution changes as discussed above. The calibrated 0.10 M HCl was added to base samples, as the titrant used is 0.10 M KOH. The final sample amount added to the titration sample varied depending on the applied current, this was to maintain the amount of titrant delivered to the sample at a reasonable 1 mL of titrant. These predicted amounts were based on the true faradaic efficiency of the BPM. Using the titrant volume at inflection point of the titration, the actual concentration of the sample was determined using the calibrated concentration of the titrant eq. 2.1.

$$c(sample) = \frac{[c\,(HCl) \times w(HCl)] - [c\,(titrant) \times V(titrant)]}{w(sample\ weight)} \quad \text{(eq. 2.1)}$$

Assessing the system for leaks.

The open circuit voltages (OCVs) were used to assess the stack for leaks, as a leak or shunt current would lead to reduced OCV values. For each of the circuits containing a membrane (circuits B-E; Figure 2.4b), the estimated OCV was calculated based on the electrolyte concentrations and composition, tested experimentally in an H-cell, and then determined for the overall BPMED system (Table 2.2). To predict OCV values for the different circuits, the Nernst potential was calculated (eq. 2.2), focusing on the concentration of the ion (X), with X_{cat} representing the species concentration on the cathode side of the ion-exchange membrane (IEM), and X_{an} representing the species concentration on the anode side. This primary transported ion is the ion that is expected to be in equilibrium across the IEM. For example, across the BPM where there is a strong acid/base on either side, we use $X = H^+$ for this circuit. A pH gradient can also be used for calculating the OCV for circuit E.

$$OCV = \frac{RT}{F}\, ln\ ln\ \left[\frac{X_{cat}}{X_{an}}\right] \quad \text{(eq. 2.2)}$$

However, when considering circuits B and C, $X = H^+$ does not represent the dominant ion in equilibrium across these circuits. For example in circuit B, the IEM used is a CEM able to transport Na^+, and the large concentrations of this species on both sides of the membrane result in

$X = Na^+$ for circuit B. Likewise, circuit C contains an AEM that selectively conducts Cl^-, allowing us to reasonably use Cl^- as our dominant transport ion.

When we compare the BPMED test platform, H-cell, and estimated values, as in Table 2.2, we see that circuits B,C, and E have values similar experimentally to what is calculated, assuming only one dominant ion setting the equilibrium membrane potential at OCV. For our circuit D, we see the H-cell agrees with the BPMED values, while the calculated values are slightly higher than either of the experimental values. This is the result of additional ions contributing to the OCV, which is not accounted for in our simple calculation.

Table 2.2: Direct comparison of values between the cells.

Circuit	Circuit Components	BPMED	H-Cell	Cal. Values
B	1 M NaCl || CEM 1 || 1 M NaOH	0.027	-0.016	0.00 V
C	1 M HCl || AEM || 1 M NaCl	-0.022	-0.019	0.00 V
D	1 M NaOH || BPM || 1 M HCl	0.784	0.789	0.83 V
E	1 M NaOH || CEM 2 || 1 M NaOH	-0.062	-0.003	0.00 V

Further system modifications

Flow cell design.

Electrochemical stacks are plagued with inefficiencies that stem from the resistance required to pass current through the system.[9, 10] To best address these various system resistance issues, we can break the BPM system into three main resistance sources; ion-exchange membranes, liquid electrolyte, and electrode surfaces. We can then see the contributions of each component to the overall system resistance and apply unique solutions to each of these category. For electrode surface resistance, a catalyst is applied to reduce the potential drop from the electrode to ions in solution.[7] For the resistance of the ion-exchange membranes, the polymer itself can be modified to allow for higher conductivity of select ions that carry the charge through the membrane. Polymers can be modified through increased polymer functionalization, however this may lead to higher swelling ratios in solution, leading to poor membrane durability.[11, 12] Finding the balance of polymer function will be discussed further in Chapter IV. For the resistance of the liquid electrolytes, there are a few options for modifying the resistance of these portions of the electrochemical stack and they involve balancing the system function and modifying the stack configuration.

The first part of electrolyte resistance stems from the conductivity of the electrolytes themselves. Electrolyte solution conductivity can vary from 0.04-0.4 S cm^{-2} depending on the concentration of the electrolyte used in the system.[13] The concentration of the system is a set parameter that is determined via systems analysis, looking at the balance of parameters such as active area, current density, membrane permselectivity, repeating units, filtration systems, etc. The balance of these parameters is often determined through the use of techno-economic analyses, considering the economics of balancing the pumps and energy load required as inputs to support the output of the desired products, say, caustic solutions as reagents. The balance of these parameters is highly system and situation dependent and are the initial steps to developing a viable electrochemical stack. Here, we are simply considering a fundamental electrochemical stack and the changes we can make at the lab scale to inform future techno-economic analyses. The parameter we can start to address is the electrolyte resistance through the modification of the stack configuration. Looking at the equation for resistance (R), we see that it consists of conductivity (κ), length (l, along the current path), and the area of the electrolyte flow channel (A).

$$R = \frac{1}{\kappa} \times \frac{l}{A} \qquad \text{(eq. 2.3)}$$

The length along the current path (l) correlates to the thickness of the spacer placed between the membranes and electrodes in a stack (Figure 2.2). Thus, it would stand to reason that to reduce the resistance of the electrolyte portion of the stack, the spacer mesh needs to be as thin as possible, ideally less than 100 μm for high current density systems.[14] However, the thinner the spacer thickness, the lower the Reynolds number (Re), as seen in eq. 2.4 where the channel width (L) is related to the density of the fluid (ρ), speed of the flow (υ), and viscosity of the solution (μ).

$$Re = \frac{\rho \upsilon L}{\mu} \qquad \text{(eq. 2.4)}$$

This laminar flow means that traditional methods of solution mixing no longer apply, resulting in concentration gradients in the flow fields as ions are no longer able to efficiently travel orthogonally away from or toward the membrane surfaces (Figure 2.8).[15]

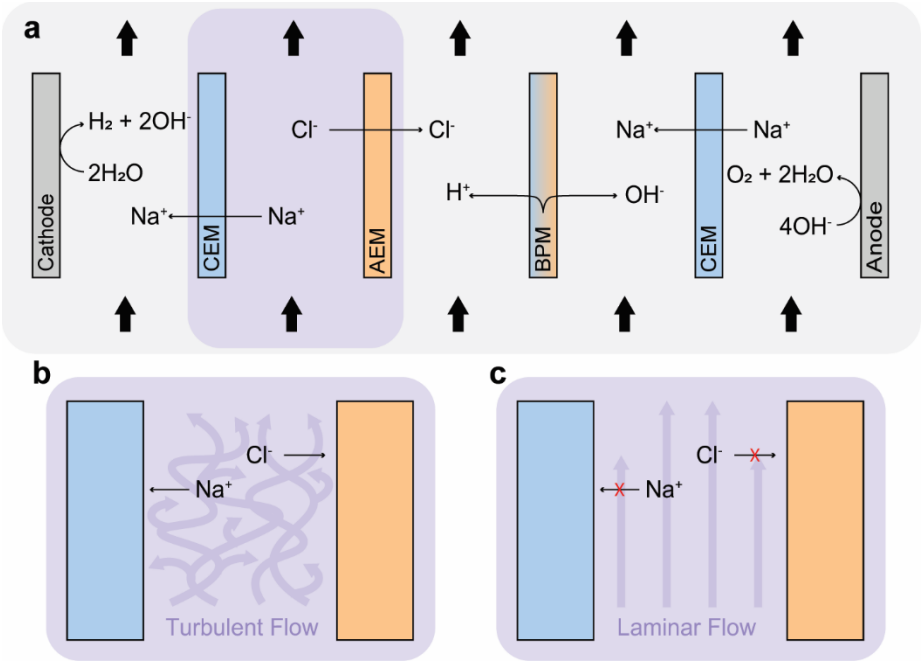

Figure 2.8: Schematic depicting the turbulent (b) and laminar flow (c) mixing in the brine compartment of an example electrodialysis system (a).

These concentration gradients result in higher resistance systems and potential membrane fouling or scaling.[16] To address the issue of laminar flow, mixing must be induced by the structure, or composition, of the mesh itself.[15, 17-21] For this, additive manufacturing was explored as a means to introduce more control over the mesh structure and design.

The method for mesh construction is known as melt electro-writing (MEW) and it is primarily utilized in the medical sciences to construct scaffolding for cell growth.[22, 23] The technique is rapidly expanding the number of materials and structures it is able to utilize, presenting a viable option for highly engineered spacers for applications like electrochemical stacks. The technique utilizes a syringe nozzle that forces melted polymer through the tip using pressure, and an electric field between the nozzle and the substrate allows for the formation of a filament jet (Figure 2.9).

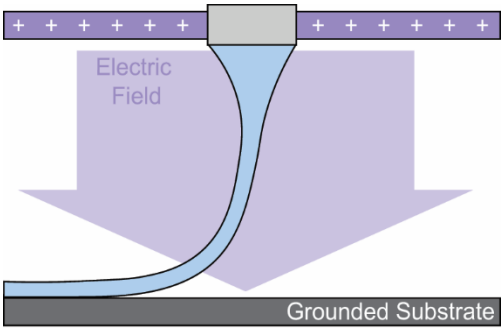

Figure 2.9: Basic schematic of MEW printing, showing the polymer melt being pulled toward a grounded substrate via an electric field as the melt is forced out of the melt nozzle.

The jetting of the filament allows for the formation of polymer fibers with highly controlled diameters of 5-50 µm.[22]

Initial flow field designs started with a proof of concept, simple structure. This structure was tested for both its manufacturability and survivability within the BPMED system. Utilizing COMSOL, the flow velocity of solution through a simplified unit cell was assessed (Figure 2.10).

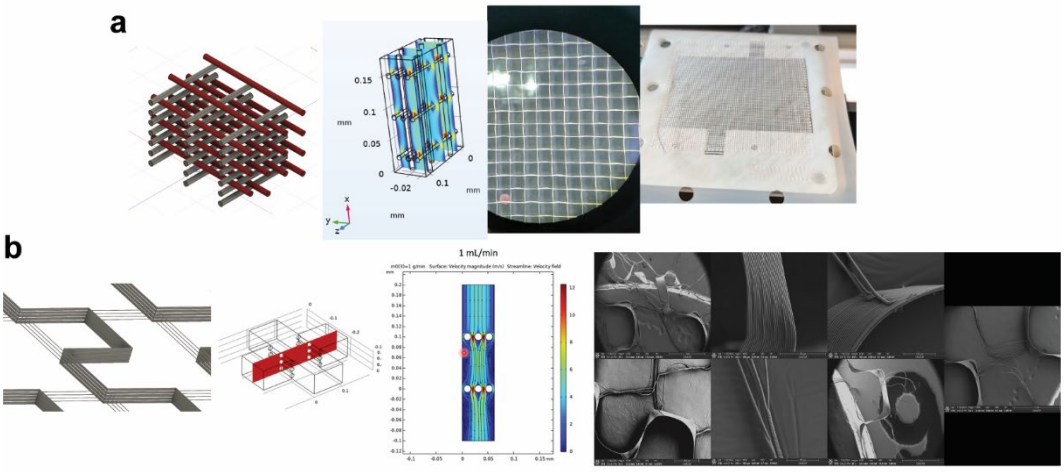

Figure 2.10: From CAD model to COMSOL flow model to MEW printed structure for a simple log stacked configuration (a) and a more complex serpentine structure (b).

These initial proofs showed that MEW printing can be utilized to manufacture large flow fields with complex geometry. Additionally, the mesh material can withstand 1 M acid and base for the duration of a polarization curve test in the BPMED system.

This project has significant potential to help address laminar flow issues as spacer mesh thickness is reduced below 100 µm. Further studies should marry the computational fluid

dynamics (CFD), or COMSOL, modeling of the orthogonal flow/mass transfer using the Sherwood numbers (*Sh*) and the cross flow power number (*Pn*) with the ability to construct fine detail scaffold with MEW printing.[16, 24, 25] MEW printing is a newly scaled technique, compared to the difficult to scale alternative additive manufacturing techniques, that holds great potential for future exploration in a wider range of materials and systems and would dramatically benefit electrochemical stacks.[26, 27]

Temperature dependence experiments.

As discussed by other researchers, the temperature of the BPM stack system is of growing importance as the system's current rises.[28, 29] However, the system presented here is not built to perform in temperatures above 35 °C. The main issue when increasing the temperature of this system is the expansion of the PTFE gaskets and the PEEK endplates. As the temperature is raised from 25 °C to 85 °C, the PTFE gaskets will expand by ~0.03 mm. Additionally, the PEEK endplates will expand by ~0.07 mm. While this doesn't sound significant, these small changes in size can lead to leakage issues in the BPMED system around gasket features, such as bolt holes and around the serpentine plate, while also varying the compression of the spacer mesh on the BPM surface. These mechanical impacts on the BPM should be studied, and the system should be modified to better tolerate higher temperature testing. Furthermore, the type of reference electrode should be considered when increasing the temperature of the experiments, as the junction potentials of the reference electrodes themselves can vary with temperature.

Conclusions

Presented here is a truly lab scale system that can be used to deconvolute electrochemical potential drops through a range of electrochemical stacks. This system is modular, can be built by any lab using the available files in the notes, and costs less than $10,000 to fully build. This platform will hopefully advance electrochemical stack engineering and understanding for future labs, with the potential for projects such as temperature studies and engineered spacers for high current density applications.

Notes

Standard Operating procedure (SOP) for BPMED: For a comprehensive guidance on the assembly, operation, and troubleshooting of the BPMED system, a SOP has been made publicly available and can be accessed via Figshare at https://doi.org/10.6084/m9.figshare.28021250.v1

CAD and 3D printing files of BPMED system components: Access via Figshare at https://doi.org/10.6084/m9.figshare.28021196.v1

Laser cutting files for gaskets and spacer mesh: Access via Figshare at https://doi.org/10.6084/m9.figshare.28021217.v1

Bridge

The system designed in Chapter II allowed for the study discussed in Chapter III. With the ability to isolate potential drops consistently in a complex electrochemical stack, testing of lab-made bipolar membranes could be expanded from the initial electrolyzer application.

CHAPTER III

COMPARING ADVANCED BIPOLAR MEMBRANES FOR HIGH-CURRENT ELECTRODIALYSIS AND MEMBRANE ELECTROLYSIS

Olivia T. Vulpin, James B. Mitchell, Lihaokun Chen, Jeonghoon Lim, Sayantan Sasmal, Nathan G. Price, Sam R. Jarvis, and Shannon W. Boettcher

From Vulpin, O. T.; Mitchell, J. B.; Chen, L.; Lim, J.; Sasmal, S.; Price, N. G.; Jarvis, S. R.; Boettcher, S. W. Comparing Advanced Bipolar Membranes for High-Current Electrodialysis and Membrane Electrolysis. *ACS Energy Letters* **2025**, *10* (2), 845-852.

Introduction

Bipolar membranes (BPMs) are composed of a polymeric anion-exchange layer (AEL) and cation-exchange layer (CEL) sandwiched together around a catalytic layer that speeds water dissociation (Figure 3.1a). These polymers are ionomers composed typically of a hydrophobic backbone functionalized with stationary charged groups, such as sulfonic acid groups for the CEL and quaternary ammonium groups for the AEL.[30] Ion-exchange layers conduct ions with opposite sign (counter-ions) to those of the charged groups bound to the backbone and exclude ions of the same sign (co-ions). With these differently charged layers, the BPM is able to maintain large pH gradients via water dissociation at the junction of the CEL and AEL, making them useful for a broad range of applications, such as electrolyzers, fuel cells, desalination, acid-base production, brine remediation, and lithium recovery, among others.[31-35] Broadly, these technological applications fall into two categories – those where electrolytes freely flow on either side of the BPM, such as in electrodialysis (Figure 3.1c) and those where the BPM is part of a membrane-electrode assembly, such as in an electrolyzer or fuel cell, and compressed under high static pressure via a rigid porous-transport layer and where the electrolyte flows along the electrodes, not interfacing directly with the BPM (Figure 3.1b).

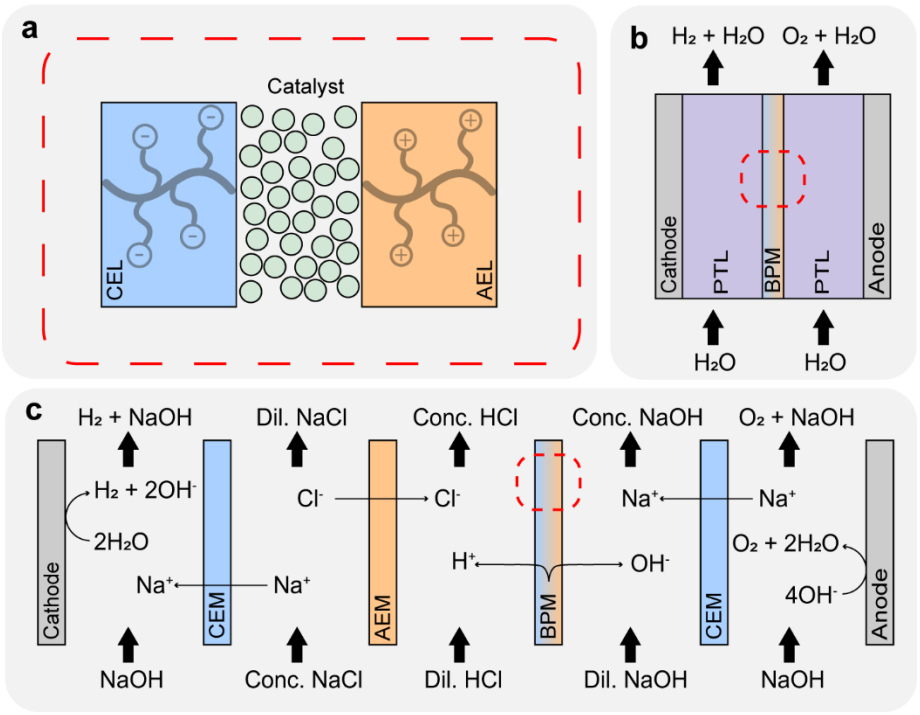

Figure 3.1: (a) Expanded view of the BPM with catalyst, cation-exchange layer (CEL), and anion-exchange layer (AEL) labeled with schematic polymer structures. **(b)** Bipolar membrane (BPM) electrolyzer (BPMWE) schematic including rigid porous-transport layers (PTLs). **(c)** BPM electrodialysis (BPMED) schematic showing the additional cation-exchange (CEM) and anion-exchange (AEM) membranes used in a single cell test system.

Membrane-electrode assemblies have become the main test platform for developing fundamental understanding of the mechanisms governing the function of BPMs, and consequently the platform that has seen the most advancement in BPM technology. BPM-containing membrane-electrode assemblies provide a system where the only mobile ions are H^+ and OH^-, unlike BPM electrodialysis systems where a range of mobile ions are present depending on the supporting electrolytes, complicating models and electrochemical analysis. Furthermore, membrane-electrode assemblies hold the BPM under spatially even, static compression, which has been shown to impact performance of the ionomer layers making up the BPM, while the freely flowing electrodialysis applications for BPM are generally unable to provide consistent static pressure to the BPM.[36-38]

The ionic resistance of the BPM can be broken into two parts, the resistance of the membrane layers (CEL and AEL) and the WD resistance, which can be equivalently cast as the WD overpotential (η_{wd}) as function of current. To address membrane layer resistance, diverse polymer structures have been proposed and synthesized to reduce counter-ion transport resistance through the membrane, while assuring that adequate co-ion selectivity of the membrane is

maintained for a given application.[39, 40] Similarly, researchers have focused on understanding the mechanisms that underly the measured η_{wd} within the BPM to inform WD catalyst designs. [8, 28, 41] Historically, η_{wd} was the largest source of voltage inefficiency in the BPM, but this is now changing due to the introduction of advanced WD catalyst designs that dramatically speed the WD reaction within the BPM.[42-45]

The precise molecular mechanisms of WD within these BPM junctions remain unsettled. Initial theories around "WD catalysis" arose from the hypothesis that weakly basic tertiary amino groups on the AEL near the BPM junction could accept and donate protons as an intermediate step in the WD reaction.[42] Recently, the BPM water electrolysis (BPMWE) architecture, where the only mobile ions are H^+ and OH^-, has been used to develop a fundamental understanding of the WD and to test and improve new WD catalysts, practically leading to >20× reduction in η_{wd}.[46] The acid-base properties of metal-oxide nanoparticles in the BPM junction are thought to be important for catalyst bilayers on the WD reaction, as evidenced by the connection between the pH of zero charge on the metal-oxide and the local pH near the AEL, or CEL, in the BPM.[41] The impact of interfacial electric field is also important; adding non-catalytic electronically conductive carbon particles at the BPM junction increases the rate of WD perhaps by focusing the electric field at the interfaces where WD occurs.[39, 47-49] In the above cases, the introduced WD catalysts are typically in the form of metal-oxide nanoparticles and are applied to the junction between the two layers of the BPM without supporting ionomer or other polymer adhesive, likely in part leading to the high performance.[39, 41, 50]

One limitation of much of the work on advanced catalyzed BPM is that they have been studied in the BPMWE platform where the BPM is under static compression in the membrane-electrode assembly (MEA) and fed pure water. As compared to a BPM in applications like electrodialysis, where the BPM is exposed to a wide range of free-flowing electrolytes, leading to possible ion contamination and low static pressure holding the BPM together. Here we study how advanced BPMs, with excellent BPMWE performance in MEAs, operate in a BPM electrodialysis (BPMED) stack.

BPMED is a technology that produces acid and base from brine (salt) solution (Figure 3.1c). Historically, the design of BPMED systems have emphasized the production of high-concentration and high-purity solutions, with little focus on the energy efficiency.[11, 14, 51] Thus, BPMED systems have generally used higher-resistance membranes that have good selectivity and

can withstand high-concentration solutions without significant co-ion leakage. However, this means that these systems have low energy efficiency, especially when driven at higher currents, in exchange for high current efficiency. Further, the BPMs used in BPMED systems have not seen dramatic development since their implementation at the industrial level in the 1960s.[51, 52]

BPMED systems can be configured with a wide range of electrolyte and membrane orientations, expanding their uses to applications including CO_2 capture, water purification, lithium and other metals separation and recovery, and even cement-clinker production.[33-35, 53] Most of these applications are at the lab-scale, with some recently emerging at the pilot-scale. The slow commercialization and scaling of these systems is in part due to the inefficiency of conventional BPMs.[35] With the introduction of advanced BPMs into BPMED systems, the energy efficiency of the system should increase, allowing for higher current-density and increased product production rate which significantly lower capital costs of emerging BPMED and related technologies.

The construction of the BPM electrodialysis and pure-water BPM electrolysis systems are related but differ in several important ways. For the BPM water electrolysis system, the BPM is subject to high and even internal pressure due to the catalyst and porous-transport layers (Figure 3.1b).[38, 54] These porous-transport layers are typically made up of multiple packed nickel, steel, or titanium-woven fiber layers or porous carbon, resulting in a relatively uniform surface. The BPM water electrolysis protocols used in this study, and for others from our team, were adopted from proton-exchange-membrane (PEM) electrolyzers.[41] For PEM electrolyzers, increased compression enhances electrolyzer performance because of improved contact between the electrically conductive porous-transport layers and the ionically conductive membrane.[55, 56] However, if compression is too high, water transport through the PEM electrolyzer membrane is impeded and the system resistance increases. [57] Despite the impacts of compression on PEM electrolyzer performance, there is little documented on the impact of compression on the BPM. This is interesting when using BPMs in BPM electrodialysis systems that can provide a range of internal pressures as the spacers and materials used in the BPM electrodialysis flow fields are changed (Figure 3.2).

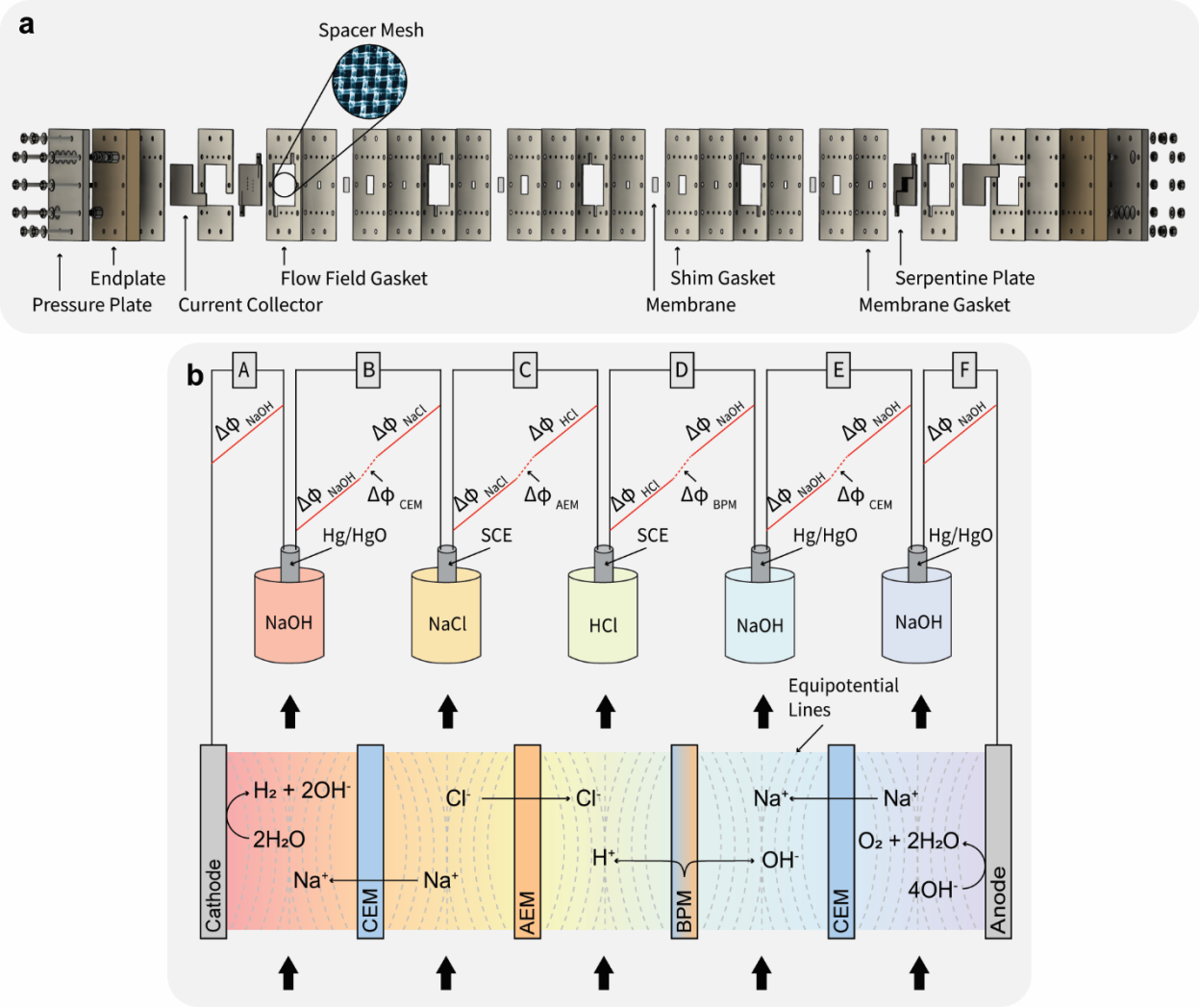

Figure 3.2: (a) Exploded schematic of the full BPMED system, with labels for the various gaskets and components of the system. **(b)** Schematic of the membrane and electrolyte layers in the BPMED stack, with the different measured potential drop circuits labeled **A** through **F** and schematic potential drops ($\Delta\phi$) within each circuit, as described also in the main text.

Within the BPM electrodialysis system, flow-field spacers are typically course, single-layer weaves of inert plastic, such as polypropylene, with weave wire diameters ranging from ~100µm to 1 mm and thus lead to uneven compression on the membrane surface.[9, 14, 20] More broadly, little is known about the ideal compression of the BPMs in BPM electrodialysis systems with regards to membrane performance, which relies heavily on the details of the BPM junction and membrane fabrication. [9, 26, 58]

In addition to the different possible effects of static pressure on the BPM, there are differences in degradation and fouling mechanisms present in BPM electrodialysis compared to

BPM water electrolysis. BPM water electrolysis is often run with pure water contacting the BPM surface, while in BPM electrodialysis the BPM is exposed to a range of differential electrolyte concentrations, compositions, and pHs. As the concentration of the solution contacting the AEL and/or CEL making up the BPM increases, the membrane is less able to exclude the transport of co-ions (via Donnan exclusion) through the respective layers.[59, 60] The unwanted transport of co-ions may lead to fouling of the catalyst at the BPM junction, contamination of adjacent solutions, shunt currents, and surface contamination of the BPM as divalent ions precipitate at the BPM surface.

With these differences in mind, we report a lab-scale BPM electrodialysis platform suitable for the study of potential drops throughout the BPM electrodialysis system via the introduction of reference electrodes to the brine, acid, base, and electrolyte feed solutions (Figure 3.3b). This platform enables the measurement of parameters such as η_{wd} to compare directly between the BPM water electrolysis and BPM electrodialysis systems. We find that the new metal-oxide water dissociation catalysts developed for use in BPM water electrolysis substantially lower the transmembrane voltage at a given current, due to lower η_{wd}, in the BPM electrodialysis systems. The absolute η_{wd}, however, in the BPM electrodialysis devices are roughly twice that of the equivalent water dissociation catalyst in the BPM water electrolysis devices at the equivalent temperatures. These results are important because they demonstrate that the fundamental principles governing the performance of water dissociation catalysts in advanced BPMs in the BPM water electrolysis system translate to the BPM electrodialysis platform, despite the BPM electrodialysis platform having co-ions present and a lower static pressure.

We also report current efficiency data for the advanced BPMs in BPM electrodialysis compared to commercial Fumasep BPM. Although the advanced BPMs were constructed with AEL and CEL designed for fuel cells and electrolyzers that typically have high proton and hydroxide ion conductivity, but lower permselectivity, current efficiency values were found to be on par with commercial Fumasep BPM. The good current efficiency found in the advanced BPM electrodialysis system, particularly at the larger water dissociation currents studied, may be due to the high efflux of protons and hydroxide ions preventing the influx of unwanted co-ions.[61] These findings thus demonstrate the feasibility of high current, next-generation BPM electrodialysis stacks. With appropriate system engineering, these membranes may lower capital expenses by

increasing the generation rate per area of acid and base for a variety of applications in water treatment, separations, and carbon-dioxide capture.

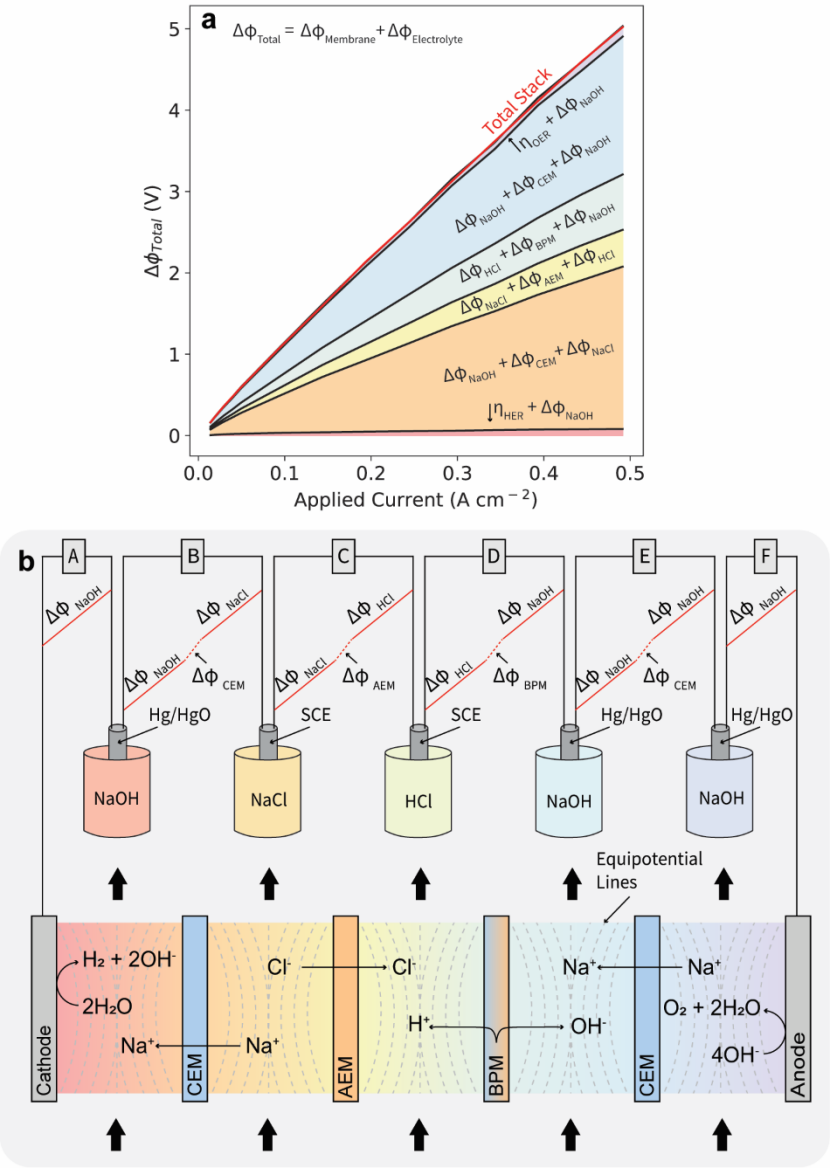

Figure 3.3: (a) Overpotential across each measured circuit throughout the BPM electrodialysis system (i.e. potential change as a function of current, relative to the open-circuit value), totaling to the measured entire system voltage (total stack) at 25 °C. **(b)** Schematic of the membrane and electrolyte layers in the BPM electrodialysis stack, with the different measured potential drop circuits labeled **A** through **F** and schematic potential drops ($\Delta\phi$) within each circuit. The $\Delta\phi$ moving from the center from one flow channel, across a membrane, and to the center of an adjacent flow channel are measured using reference electrodes in the reservoirs feeding each electrolyte flow of the overall stack. The color gradients schematically represent the potential gradients in each section of the electrodialysis stack. We take each reservoir (represented as the uniform-colored cylinders) as equipotential to the electrolyte at approximately the midpoint of the flow channel represented by the vertical dashed line. An ohmic potential drop is present across the electrolyte region and the membrane region of the system. The measured steady-state voltage changes also include contributions from concentration polarization in addition to contributions from electric-potential drops driving migration. Circuits **A** and **F** further include the reaction kinetic overpotentials which are not important in this study but contribute to the overall cell voltage.

Results/Discussion

High-current BPM electrodialysis test cell design and operation.

A BPM electrodialysis test cell was designed with several degrees of adjustability and monitoring capabilities to aid in understanding the BPM electrodialysis system. This approach allows for the overall BPM electrodialysis system to be broken down into six different circuits that record the potential drop across specific features of the BPM electrodialysis system (Figure 3.3). To record these individual circuits, reference electrodes were placed in the external solution reservoirs feeding the respective five solutions circulating through the BPM electrodialysis system. Because current doesn't pass through the electrolyte in the tubing connecting the cell to the reservoirs, these are taken to be roughly equipotential and at an electric potential that is approximately equal to the average electric potential of the electrolyte flowing through the spacer-filled flow-field medium between each set of membranes.

Given this measurement scheme and approximation for electric-potential breakdown, the total potential changes relative to the open-circuit value, as a function of current, can be further broken down into their electrolyte, membrane, or reaction overpotentials, depending on the circuit measured (Figure 3.3b). Of particular interest to this study is Circuit D, which contains the BPM, and thus the contribution of η_{wd}. Circuit D can be broken down into the overpotential across the BPM ($\Delta\phi_{\mathrm{BPM}}$), the acid solution ($\Delta\phi_{\mathrm{HCl}}$), and the base solution ($\Delta\phi_{\mathrm{NaOH}}$).

$$\Delta\phi_{\mathrm{total,D}} - \Delta\phi_{\mathrm{total,D,OCV}} = \Delta\phi_{\mathrm{BPM}} + \Delta\phi_{\mathrm{HCl}} + \Delta\phi_{\mathrm{NaOH}} \quad \text{(eq. 3.1)}$$

Note that terms $\Delta\phi_{\mathrm{HCl}}$ and $\Delta\phi_{\mathrm{NaOH}}$ each represent one half of the total electric potential drop across the flowing electrolyte regions, and that the open circuit potential (OCV) for this circuit is subtracted from the total potential. The potential drops $\Delta\phi_{\mathrm{HCl}}$ and $\Delta\phi_{\mathrm{NaOH}}$ can be calculated from:

$$\Delta\phi = iR \quad \text{(eq. 3.2)}$$

The resistance (R) is calculated from the known conductivity (κ), length (l, along the current path), and A the area of the electrolyte flow channel.

$$R = \frac{1}{\kappa} \times \frac{l}{A} \quad \text{(eq. 3.3)}$$

To calculate the resistance of the electrolyte solutions (HCl and NaOH) in circuit D and the contributions of $\Delta\phi_{\mathrm{HCl}}$ and $\Delta\phi_{\mathrm{NaOH}}$, κ for each is calculated from the ion concentrations of each solution and the reported molar conductivities.[13] It was assumed that the reference electrodes were equipotential with the electrolyte exactly half-way across the spacer between the two membranes along the path of the current flow, which here is equal to half the thickness of the spacer mesh used in the BPM electrodialysis system. Because the spacer mesh reduces the open volume of the electrolyte available for ionic current conduction, we define $A_{\mathrm{electrolyte}}$ = *geometric area* × *fraction open area*. We note that these calculations do not take into account boundary layer effects and associated concentration polarizations.[62] Thus the analysis implicitly assumes the turbulence of the spacer mesh, flow rate, and pH gradient are sufficient to prevent significant boundary-layer effects. Further coupled fluid dynamics and migration/diffusion transport modelling of these systems will be useful.

To obtain $\Delta\phi_{\mathrm{BPM}}$, the $\Delta\phi_{\mathrm{HCl}}$ and $\Delta\phi_{\mathrm{NaOH}}$ values were subtracted from $V_i - V_{ocv}$ measured across the reference electrodes. The term $\Delta\phi_{\mathrm{BPM}}$ can be further broken down into the potential drop across the solid CEL and AEL ionomer electrolytes ($\Delta\phi_{\mathrm{CEL}}$ and $\Delta\phi_{\mathrm{AEL}}$; respectively) and the overpotential for water-dissociation (η_{wd}).

$$\Delta\phi_{\mathrm{BPM}} = \eta_{\mathrm{wd}} + \Delta\phi_{\mathrm{CEL}} + \Delta\phi_{\mathrm{AEL}} \quad \text{(eq. 3.4)}$$

From the $\Delta\phi_{\mathrm{BPM}}$ values, membrane conductivities, determined via H-cell measurements, and thicknesses (l) were used to calculate and subtract $\Delta\phi_{\mathrm{CEL}}$ and $\Delta\phi_{\mathrm{AEL}}$ to provide η_{wd}.

$$\eta_{\mathrm{wd}} = \Delta\phi_{\mathrm{total,D}} - \Delta\phi_{\mathrm{HCl}} - \Delta\phi_{\mathrm{NaOH}} - \Delta\phi_{\mathrm{CEL}} - \Delta\phi_{\mathrm{AEL}} \quad \text{(eq. 3.5)}$$

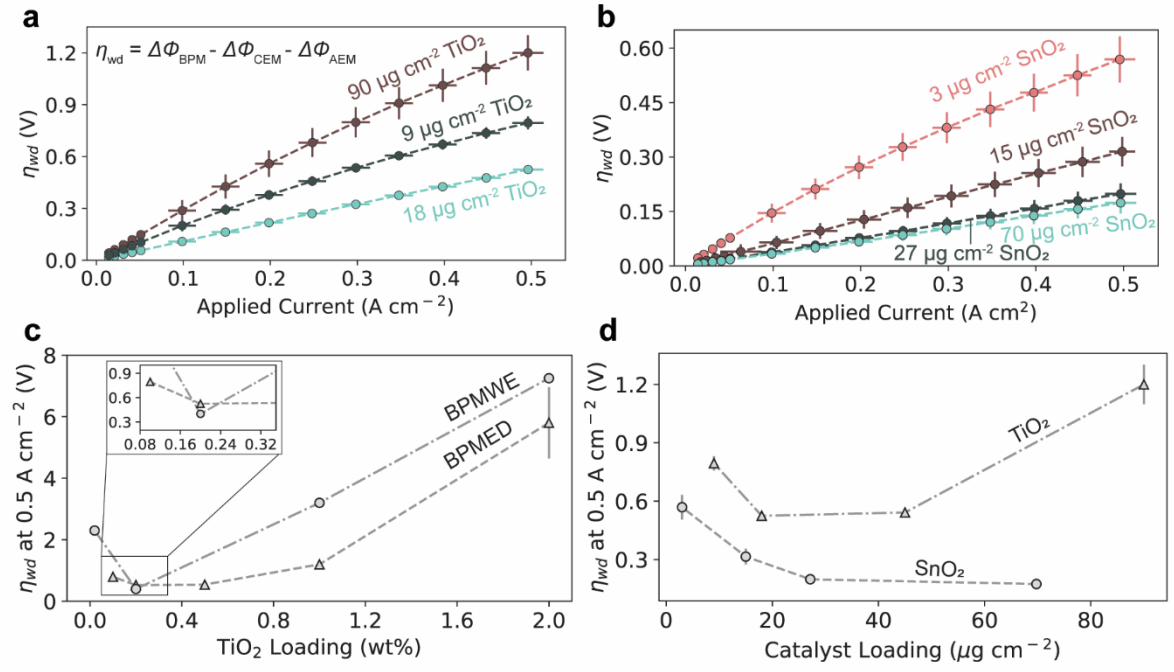

Figure 3.4: Effect of catalyst type and loading. (a) Polarization curve showing η_{wd} in the BPMED system with TiO_2 WD catalyst loading varied. **(b)** Polarization curve depicting η_{wd} in the BPMED system as SnO_2 nanoparticle catalyst loading is varied. **(c)** The η_{wd} at 0.5 A cm^{-2} as TiO_2 catalyst loading is varied for BPM water electrolysis (circle) and BPMED (triangle) systems. **(d)** The η_{wd} at 0.5 A cm^{-2} as catalyst loading for TiO_2 and SnO_2 is varied for the BPMED system. All BPMED and BPM water electrolysis runs were collected at 25 °C in triplicate and error bars are shown as one standard deviation in cases where they are larger than the symbols.

Comparing performance via η_{wd}.

Using the presented BPM electrodialysis platform, η_{wd} was compared between the BPM electrodialysis and BPM water electrolysis systems. Controlling the WD catalyst loading following the procedures described previously,[39] the catalyst loading was found to impact η_{wd} following similar trends between the two system types, where an increase in TiO_2 catalyst loading in a range of ~0-100 μg cm^{-2} led to reduced η_{wd} (Figure 3.4a). Similar results were found for recently reported SnO_2 nanoparticle paste catalyst (Figure 3.4b).[7, 39]

To elucidate performance trends between the BPM water electrolysis and BPM electrodialysis systems, the η_{wd} values at 0.5 A cm^{-2} were plotted versus TiO_2 catalyst loading (Figure 3.4c). Both the BPM water electrolysis and electrodialysis experiments revealed a characteristic U-shape observed previously with optimal TiO_2 loading of ~ 20 μg cm^{-2}.[39] This result suggests that advanced BPMs developed, and fundamentally understood, in a BPM water electrolysis system can be translated to more-complex systems like BPM electrodialysis, allowing

BPM water electrolysis systems to serve as an adequate development platform for BPMs in BPM electrodialysis systems.

The deviations in U-shape trends seen in Figure 3.4c could be due to an inconsistent BPM construction at the lab-scale, impacts of co-ions from the soluble electrolytes on the physics of the BPM junction, or a difference in the static pressure on the BPM. Co-ion contaminants would increase ionic conductivity within the BPM junction, thus affecting the electric-field distribution by concentrating it more at the interfaces with AEL and CEL.[63] This could result in a weaker dependence of η_{wd} on catalyst loading, similar to what is observed when adding electrically conductive media to the BPM junction.[39] Changes in static pressure on the BPM may also lead to reduced water transport through the BPM as pressure is increased, following the trends seen in proton-exchange membrane electrolyzers and when determining conductivity of ion-exchange membranes.[56, 57] Further, if reduced pressure leads to a less-compact BPM junction, the distance over which the electric potential drops will increase and the local electric field that is hypothesized to control water preorganization will decrease.[64] Deconvoluting these possible differences, however, is not yet possible.

We also studied a new low-temperature, nano-SnO_2 paste WD catalyst. A shallower U-shape curve of η_{wd} versus loading was observed (Figure 3.4d).[7] Like in BPM water electrolysis, the optimal loading of the SnO_2 was higher than for TiO_2. The SnO_2 catalyst is more electrically conductive than the TiO_2 catalyst, perhaps the reason for the shallower U-shaped curve.

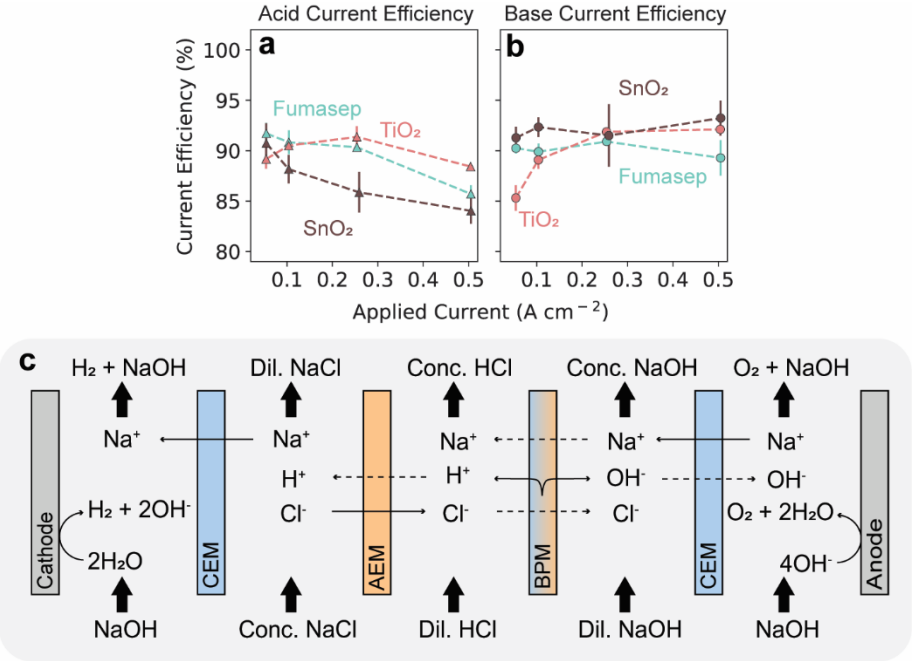

Figure 3.5: Current efficiency for **(a)** acid and **(b)** base production as the current is varied for a Fumasep BPM in the BPM electrodialysis system (blue), TiO_2 catalyst-coated BPM (pink), and SnO_2 catalyst-coated BPM (brown). All runs were collected at 25 °C in triplicate and error bars are shown as one standard deviation in cases where they are larger than the symbols. **(c)** Possible mechanisms of ion-cross over and shunting currents are represented by dashed lines a BPMED schematic.

Comparing BPM performance via current efficiency.

Historically, production of a desired product (i.e. selectivity) was the primary goal of BPM electrodialysis, but this often came at the expense of energy efficiency.[11, 14] One important measure of selectivity is current efficiency. Here, current efficiency is defined as the ratio of proton (or hydroxide ion) production experimentally versus the predicted production rate at a specific current density. This generation rate (G) can be calculated using eq. 3.6, where the current (i) passed through the system is converted to mol/s using the number of electrons transferred in the reaction (n) and Faraday's constant (F).

$$G = \frac{i}{nF} \qquad \text{(eq. 3.6)}$$

The generation rate is then used to determine the theoretical concentration change (ΔC_{theo}) based on the amount of time (t) current was passed through the stack. The theoretical concentration

change can be compared to the experimental concentration change (ΔC_{exp}), as determined via titration, as described in eq. 3.7-3.9, providing a percent current efficiency (*CE*).

$$\Delta C_{\text{theo}} = G \times t \quad \text{(eq. 3.7)}$$

$$\Delta C_{\text{exp}} = C_f - C_i \quad \text{(eq. 3.8)}$$

$$\frac{\Delta C_{\text{theo}}}{\Delta C_{\text{exp}}} \times 100\% = CE \quad \text{(eq. 3.9)}$$

We measured current efficiency using the system described above to quantify the performance of BPMs. For this, the BPMED system was held at a constant current for 30 min, with base and acid samples titrated before and after this current hold to determine the change in pH in both the acid and base reservoirs associated with the total charge passed.

Figure 3.5 shows the current efficiency of the BPMED system for the optimally loaded TiO_2 BPM and SnO_2 BPM, as compared to a common commercial BPM from Fumasep. The TiO_2 BPM showed current efficiency values of ~90% for both acid and base solutions across a current density range of 0.05 - 0.50 A cm^{-2}, while the SnO_2 BPM showed current efficiency values of ~87% and 90% for acid and base, respectively (Figure 3.5a and 3.5b). A current efficiency value of ~90% is consistent with the findings of Lucas et al., who used a similar BPMED system.[65]

Compared to Fumasep's BPM current efficiency values, the TiO_2 BPM performed slightly worse at low currents, 0.05 - 0.10 A cm^{-2}, and improved at higher currents, 0.25 - 0.50 A cm^{-2}. This trend could be due to higher flux of generated protons and hydroxide ions from the BPM junction at the higher currents, or related to the ionomer materials themselves.[66] As current increases, the efflux of proton- and hydroxide-ion mobile species likely impedes the influx of co-ions, due to concentrated ion-ion interactions, thus increasing current efficiency at higher currents.[67] This is an effect that we have previously noted, but requires further study to fully understand.[61] Lucas et al. also noted reduced current efficiency at lower currents, attributing the trend to increasing co-ion transport across the BPM at these lower currents. Similarly, the SnO_2 BPM showed similar base current efficiency trends to TiO_2, but showed a reduced acid current efficiency compared to both TiO_2 and Fumasep's BPM.

Substantial current efficiency loss can be expected given the unoptimized individual AEM and CEM that are used along with the BPM in the BPM electrodialysis test platform. Because of

the four-membrane configuration of this BPM electrodialysis platform, current efficiency can also be reduced by ion-leakage across the supporting AEM and other two CEMs in the overall BPM electrodialysis system (Figure 3.5b). The loss of protons across the supporting AEM, for example, can lead to reduced acid current-efficiency values. The leakage of protons is difficult to prevent, and may explain the reduced current efficiency of the acid solution at high currents, compared to the basic solution current efficiency. If the BPM ion-leakage was equivalent, then the acid and base solution current efficiencies should be the same. The optimization of the supporting AEM and CEM must be addressed in conjunction with advanced BPM integration in BPM electrodialysis device cells and stacks. While the use of more-permselective membrane layers in the BPM itself might lead to further decreased co-ion crossover and thus higher current efficiencies as well, these initial findings show that the use of CELs and AELs developed for BPM water electrolysis applications can perform well in BPM electrodialysis systems, especially at high-current densities.

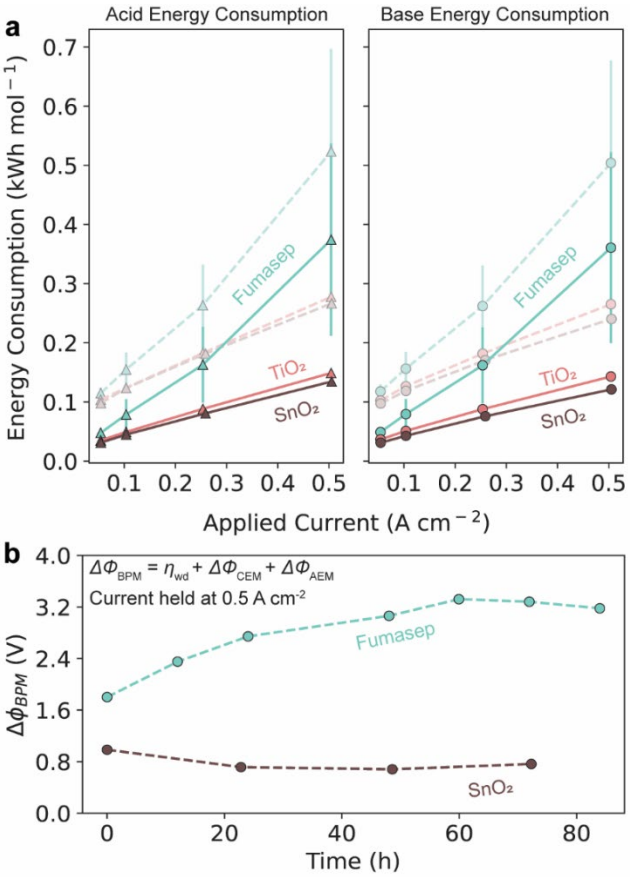

Figure 3.6: (a) Energy consumption of commercial Fumasep, TiO_2, and SnO_2 BPMs in the BPM electrodialysis system for the production of either H^+ (acid) or OH^- (base) plotted versus applied current. The energy consumption for a single repeating cell in the overall stack is represented as solid, bold lines, while the total stack containing a single cell is represented as dashed, faded lines. Data collected in triplicate with error bars shown as one standard deviation in cases where they are larger than the symbols. **(b)** BPM transmembrane potential ($\Delta\Phi_{BPM}$) versus time for commercial Fumasep and SnO_2 catalyst-coated BPM held at 0.5 A cm^{-2} in the BPM electrodialysis system. All runs were collected at 25 °C. The new BPMs are substantially superior in terms of transmembrane voltage compared to the baseline Fumasep BPM.

Overall impact of performance gains.

Compared to the commercial Fumasep BPM, both the TiO_2 and SnO_2 catalyst-coated BPMs performed dramatically better with respect to energy consumption (Figure 3.6a), with a nearly two-fold decrease in energy consumption for the production of H^+ or OH^- product. Furthermore, the durability of the SnO_2 catalyst-coated BPM is improved over the Fumasep BPM in the BPMED system tested, with Fumasep showing a degradation of ~2.11 mV h^{-1} and SnO_2 showing a degradation of ~ 0.31 mV h^{-1} (Figure 3.6b). With these improvements, the catalyst-coated BPM can operate at higher current densities, while also providing higher product output at competitive efficiencies without compromising durability, may enable economical applications in electrochemical stack systems, like CO_2 electrolysis and brine remediation. However, detailed and application specific techno-economic analyses are required to fully understand the impact of catalyst-coated BPM on the viability of BPM containing technologies.

Conclusion

In summary, we have reported the initial successful translation advanced, catalyzed BPMs from membrane-electrode assemblies in electrolyzers to BPM electrodialysis systems –metal-oxide catalysts optimized in one system also improve performance in the other system. The new catalyzed BPM provided current efficiency values for acid-base generation that exceeded those found for common commercial Fumasep BPM at current-densities above 0.2 A cm^{-2}, while requiring only roughly half of the driving voltage across the BPM. We also report a simple design for BPMED test platform that allows for the isolation of electrostatic potential drops across individual membranes in the system, allowing for the measurement of important characteristics like η_{wd} within the BPMED system. While further research is required to better understand the impacts of compression and possible co-ion fouling mechanisms in BPMWE-based BPM, the increased current densities in part enabled by the advanced BPMs are expected to facilitate broader adoption of BPM-based electrochemical technologies in electrodialysis-type platforms.

Experimental Methods

Membranes and catalysts.

The cation-exchange membranes used include Nafion 212 and Selemion CMV-N. The anion-exchange membrane was Versogen PAP-TP-85. Nafion membranes were conditioned by pre-cutting the membranes into 1.5-cm-wide strips, removing the backing material, and letting rest in deionized (DI) water for at least 24 h. Samples were moved to new DI water solution for storage. Selemion was delivered in a hydrated state and stored in 1.0 M aq. NaCl solution. Versogen membranes were cut into 1.5 cm wide strips, the backing was removed, and the membrane was placed into 0.50 M aq. KOH solution for 8 h, then transferred to fresh 0.50 M KOH solution for storage. The Versogen membranes were allowed to rest for at least 24 h before use.

For the TiO_2 catalyst, Aeroxide TiO_2-P25 was purchased from Sigma Aldrich. TiO_2 catalyst solutions were made by dispersing the desired amount of TiO_2 powder in 1:1 mass ratio IPA:H_2O, then sonicated for at least 4 h. Typically, a high concentration solution, between 2.0-10 wt% TiO_2, was made and dilutions were taken from this mother solution. The diluted concentration range was between 0.02 and 2.0 wt% TiO_2.

For the SnO_2 catalyst, $SnCl_4 \cdot 5\ H_2O$ was purchased from Sigma Aldrich. SnO_2 catalyst solutions were made by dissolving $SnCl_4 \cdot 5\ H_2O$ in DI water at room temperature with a final solution concentration of 0.05 M. This solution was refluxed in an oil bath at 90-95 ^oC for 20 min. Once refluxed, the solution changes from clear to milky white, and the solution is left to cool at room temperature. The solution is then centrifuged for 5 min at 7,000 rpm, the supernatant discarded and replaced with DI water and centrifuged again. The centrifuging steps were repeated 5 times and at the end the supernatant is remove and the remaining white paste is stored and used to make catalyst solutions, ensuring the paste does not dry during storage. The spin-coat solutions were made by dissolving a desired amount of SnO_2 paste in 1:1 mass ratio IPA: H_2O; this solution was then left to sonicate for ~8 h. Typically, a high-concentration solution, around 5.0 wt%, was made and dilutions were taken from this mother solution. To accurately determine the wt% of SnO_2 in the mother solution, a drop of solution was pipetted onto a pre-weighed glass slide and allowed to dry on a hot plate for 2 h. The glass slide was then weighed again, and the solid content of the initial solution determined. The dilution concentration range was between 0.2 and 5.0 wt% SnO_2.

Advanced BPM fabrication.

BPM were constructed using Nafion (CEL) and Versogen (AEL). The CEL was taped to a glass slide, exposing a 1.2×1.2 cm^2 area. This assembly was then placed on a spin coater. The desired weight percent catalyst solution was dropped onto the membrane surface and spun off at 3,000 rpm for 30 s. The spin-coat solutions were composed of the desired catalyst and a 1:1 mass ratio IPA:H_2O solution. Once coated, the CEL was removed from the glass slide and layered with the AEL. Storage of the inks is typical, but BPMs are made fresh for each run.

Determining conductivity of Nafion and Versogen.

Conductivity measurements were determined using an H-cell equipped with Luggin capillaries, following the methods used by Slade et al. for assessing Nafion conductivity.[68] Measuring the potential between the two reference electrodes while stepping the current from 5 – 100 mA cm^{-2}, the resistance of the cell can be determined using Ohm's law ($V = IR_{cell}$). Data was collected for H-cells with and without the membrane in place allow for the electrolyte potential drop to be corrected for. The Nafion cells used 1 M H_2SO_4 and standard calomel reference electrodes, while the Versogen TP-85 test cell used 1 M NaOH and mercury/mercury oxide reference electrodes.

To determine the membrane resistance ($R_{membrane}$) from the H-cell data, the average of the H-cells without a membrane ($R_{electrolyte}$) was subtracted from the average of the membrane containing H-cells (R_{cell}), following eq. 3.10.

$$R_{membrane} = R_{cell} - R_{electrolyte} \quad \text{(eq. 3.10)}$$

From $R_{membrane}$, the area resistance (R_A) can be determined through eq. 3.11, utilizing the area of the H-cell opening for area (A_{cell}).

$$R_A = R_{membrane} \times A_{cell} \quad \text{(eq. 3.11)}$$

The membrane conductivity ($\kappa_{membrane}$) can then be determined through eq. 3.12, using the thickness of the membrane (l), determined using SEM imaging.

$$\kappa_{membrane} = \frac{l}{R_A} \quad \text{(eq. 3.12)}$$

The values obtained for κ_{Nafion} were 0.020 S cm^{-1} and $\kappa_{Versogen}$ were 0.016 S cm^{-1}. These values are slightly lower than those found in literature, but are close to the expected values for these two commercially available membranes.[68-71]

The potential drop across the solid CEL and AEL ionomer electrolytes ($\Delta\phi_{CEL}$ and $\Delta\phi_{AEL}$, respectively) were then determined using ($\kappa_{membrane}$) following eq. 3.13 and 3.14, respectively. Where I equals the current at a given potential, l represented the membrane thickness, and A_{BPMED} is the active area in the BPM electrodialysis system.

$$\Delta\phi_{CEL} = I \times \frac{1}{\kappa_{Nafion}} \times \frac{l}{A_{BPMED}} \quad \text{(eq. 3.13)}$$

$$\Delta\phi_{AEL} = I \times \frac{1}{\kappa_{Versogen}} \times \frac{l}{A_{BPMED}} \quad \text{(eq. 3.14)}$$

Calculations for assessing energy consumption.

Energy consumption is defined here as the energy required to produce the desired product. To determine these values, the energy consumption required to produce H^+ (or OH^-) was found by titrating the acid (or base) solutions to determine the actual concentration change (ΔC_{exp}) over a period of time (t). Following eq. 3.15, where the current applied (I) to the system and the resulting potential across a single cell or the total stack containing a single cell (V), energy consumption was determined as (Figure 3.7):

$$\frac{(t \cdot I \cdot V)}{\Delta C_{exp}} = \text{energy consumption per mol} \quad \text{(eq. 3.15)}$$

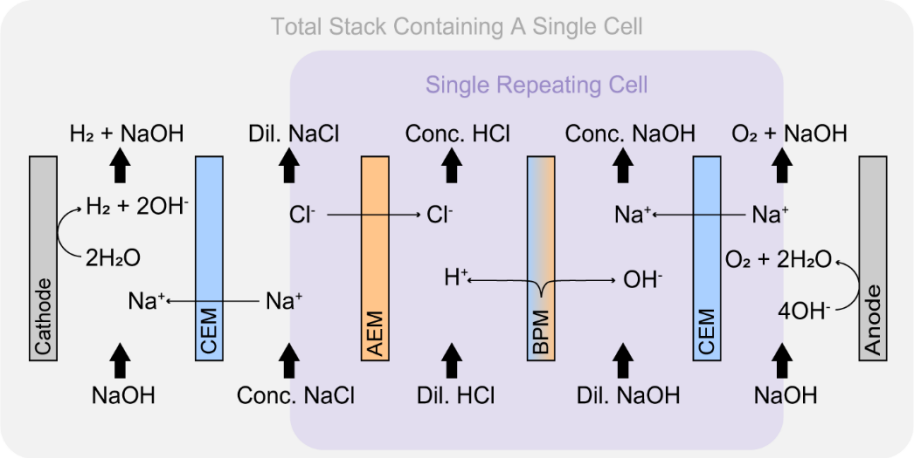

Figure 3.7: Schematic showing a single repeating cell (purple) and a total stack containing a single cell (grey).

Procedure for stability test.

For durability testing, the BPM electrodialysis stack was assembled with the desired BPM and the system reservoirs were filled with 1.0 L of 1.0 M NaOH for the catholyte and anolyte streams, 1.0 M NaCl for the brine stream, 1.0 M HCl for the acid stream, and 1.0 M NaOH for the base stream. The current density was set to 500 mA cm^{-2} and held for 12-20 h. After the 12-20 h, the current and solution flows were halted, the solutions were exchanged for fresh solutions, and the 500 mA cm^{-2} was reapplied. The solutions were replenished every 12-20 h for a total of 100 h. Once complete, the system was disassembled, and the BPM was stored for post-mortem analysis. The $\Delta\varphi_{BPM}$ data for the first 1 h after replenishing the reservoir solutions was averaged and plotted versus time, this allowed for nominally the same electrolyte concentrations between measurements.

Post-mortem assessment of SnO_2 BPM from stability test.

To assess the potential for co-ion and counter-ion crossover and accumulation in the BPM during the stability test, the BPM was freeze fractured and the BPM layers were assessed in the active area. Freeze fracturing allowed for a clean edge, that showed both the CEL and AEL, to be examined, without the crushing damage of cutting the BPM with a razor or scissors. For freeze fracturing, the BPM was dabbed dry with a Kimwipe and then placed in liquid nitrogen for 5 min. Using tweezers, the submerged BPM was pressed against the bottom of the dewar and forced to crack. A cracked edge across the active area of the BPM is located and positioned edge up on a

90-degree SEM mount, held on with carbon tape. Using an Apreo 2 SEM, the edge of the cracked BPM is imaged using an EDS detector. From the EDS line scan images, there is a clear transition between the CEL (fluorinated Nafion) and AEL, with an increase in Sn counts at the junction of the two polymer layers (Figure 3.8). Sections of the line scan were then assessed for atom % for a approximate comparison of three samples from the post-mortem BPM, pristine Versogen, and pristine Nafion (Table 3.1). From the data collected, there was a slight increase in chloride presence in the AEL of the post-mortem BPM, and a slight increase in sodium presence in the CEL.

Table 3.1: Atom % averaged for three different EDS line scans.

Element	BPM AEL	BPM CEL	BPM Junction	Pristine Versogen	Pristine Nafion
Carbon	91.44 +/- 1.32	31.68 +/- 2.35	43.16 +/- 9.71	84.87 +/- 3.29	34.72 +/- 3.91
Oxygen	0.73 +/- 0.37	5.04 +/- 0.30	6.25 +/- 1.66	10.55 +/- 3.58	5.07 +/- 1.06
Fluoride	4.79 +/- 0.90	61.05 +/- 1.82	46.45 +/- 6.32	3.02 +/- 0.45	59.88 +/- 3.65
Sodium	0.03 +/- 0.04	2.14 +/- 1.33	1.22 +/- 0.85	0.05 +/- 0.09	0.18 +/- 0.22
Chloride	3.00 +/- 0.12	0.06 +/- 0.01	1.37 +/- 0.32	1.16 +/- 0.49	0.15 +/- 0.26
Tin	0.00 +/- 0.01	0.03 +/- 0.03	1.56 +/- 1.27	0.34 +/- 0.52	0.00 +/-0.00

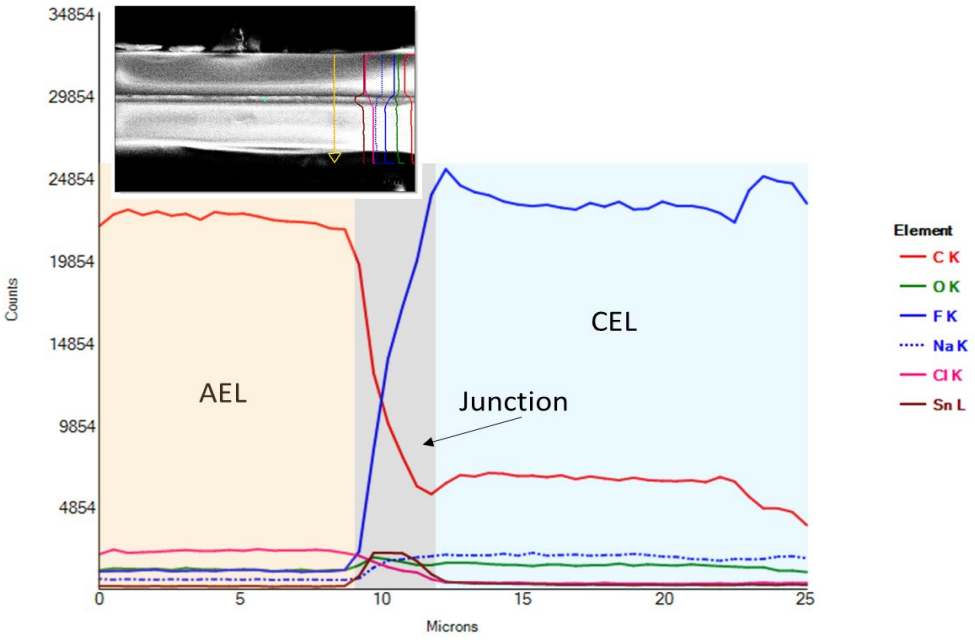

Figure 3.8: EDS line scan data of the SnO_2 BPM from the stability run, assessing the edge on BPM layers for carbon (C), oxygen (O), fluorine (F), sodium (Na), chloride (Cl), and tin (Sn). Splitting the line scan into three sections, anion-exchange layer (AEL, orange), BPM junction (grey), and cation-exchange layer (CEL, blue).

Comparison of Total Cell Potential.

The total applied potentials for three independent Fumasep BPM and 70 µg cm^{-2} loading SnO_2 BPMs were compared (Figure 3.9). It is of note that the total cell potential for these systems are quite high, owing to the unoptimized electrode chemistry of the BPMED system used and the unoptimized supporting membranes.

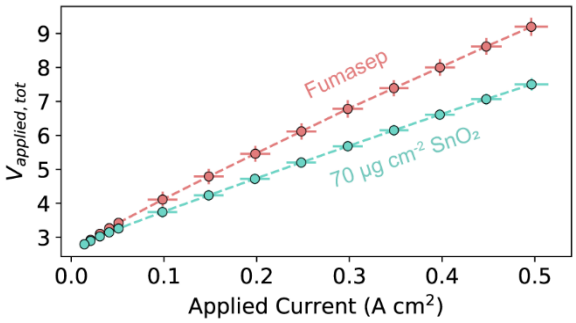

Figure 3.9: Polarization curve depicting total cell potential ($V_{applied,tot}$) versus applied current for a commercially available Fumasep BPM and the best performing SnO_2 catalyst loading (70 µg cm^{-2}). Data was collected in the BPMED system at 25 °C in triplicate.

Bridge

Chapter III outlines the initial application of advanced, catalyzed bipolar membranes in complex electrochemical stacks. In this initial investigation, the test electrodialysis system was designed to hold the bipolar membrane under mild compression, preventing mechanical issues. However, to better explore the use of catalyzed bipolar membranes outside of electrolyzer applications, these mechanical issues must be addressed. Chapter IV explored the potential causes and solutions to the mechanical delamination and blistering of catalyzed bipolar membranes.

CHAPTER IV

INVESTINGATING ADHESION BETWEEN ADVANCED BIPOLAR MEMBRANE LAYERS.

Olivia T. Vulpin, Ben Indeglia, James B. Mitchel, Sayantan Sasmal, Karen Winey & Shannon W. Boettcher

This chapter contains unpublished data on membrane adhesion and the polymeric interactions that might lead to delamination or blistering issues. Membrane manufacturing and testing was carried out by Olivia Vulpin, James Mitchell, and Sayantan Sasmal in the Boettcher lab. Membrane imaging and fundamental polymeric analysis was carried out by Ben Indeglia in the Winey lab.

Introduction

Bipolar membranes (BPMs) are a type of ion-exchange membrane used to establish a pH gradient in an electrochemical system. An ion-exchange membrane is a hydrated polymer with two distinct domains, hydrophilic and hydrophobic.[72, 73] The polymer's structure has a generic hydrophobic backbone that will orient to form the hydrophobic domain, and the polymer backbone is decorated with charged functional groups that will protrude into the hydrophilic domain (Figure 4.1).

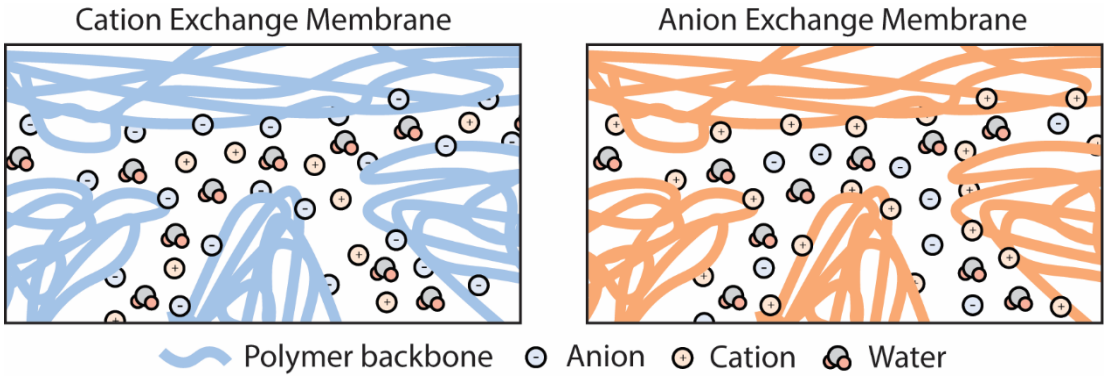

Figure 4.1: Schematic depicting the hydrophilic and hydrophobic domains of a generic cation exchange membrane and anion exchange membrane, with the orientation of functional groups toward the hydrophilic domain and the sequestration of the polymeric backbones in the hydrophobic domain.

The type of functional group will determine the ions that can pass through the hydrophilic domain when migration is induced by an electric field. Polymers containing functional groups such as quaternary ammonium groups will promote the passage of anions due to the positive nature of the functional group.[74] These polymers are known as anion-exchange membranes (AEMs). Polymers that contain negatively charged functional groups, such as sulfonic acid groups, are known as cation-exchange membranes (CEMs).[75] A BPM is a combination of both ion-exchange membrane types, having a region containing negative functional groups, like a CEM, and a region containing positive functional groups, like an AEM. With these two regions, a BPM must split water to pass current through the membrane, thus producing protons that will travel toward the cathode and hydroxide ions that will travel toward the anode.

Many sectors are looking to electrify manufacturing to achieve the decarbonization and sustainability goals set for 2050.[76] Electricity allows for the energy requirements of manufacturing to move from being fossil fuels to renewables. Of particular interest are electrochemical systems that present electrical solutions to chemical manufacturing, while also presenting new and novel means of recycling and waste management, which align with other sustainability goals.[51]

Electrochemical devices have witnessed remarkable progress in recent years, with particular emphasis on the development and advancement of bipolar membranes (BPMs).[30] BPMs are an essential component for many of these electrochemical devices, allowing for systems to perform a wide gamut of chemistries, from H_2 production to cement production to acid and base recycling.[31, 34, 35, 51, 53] Despite this range of applications, the BPMs used across these diverse systems are generic and have little to no optimization for specific applications.[53] This lack of optimization leads to poor performance across applications, whether that performance is based on energy efficiency or product purity. This lack of optimization is stifling the adoption of BPM based systems. As the scope of BPM applications expands, it becomes imperative to investigate how BPMs function under the distinct stressors diverse systems, allowing for the optimization of BPM performance for broader industrial applications and more readily specialized BPM for specific applications.

With increased research focused on advancing BPMs, a wide range of polymers and catalysts have emerged to address system fouling issues, system resistance issues, and other

functional problems. [31, 39, 40, 50, 77] With a suite of advanced CEM and AEM polymers and catalysts, there is a wide range of possible BPMs to construct and tailor for specific applications. Here we explore a range of commercially available CEM and AEM combinations, assessing their inherent compatibility. Finding that laminating commercial AEM and CEM layers has generally poor adhesion, which can lead to blistering and delamination when a BPM is placed in some electrochemical systems, like a free-flowing electrodialysis system, or a bubble forming CO_2 electrolyzer. Furthermore, adhesion is made worse when a catalyst layer is introduced to the BPM junction, interrupting the electrostatic forces holding the AEM and CEM together (Figure 4.2). To address this delamination issue, we explore a range of options from mechanical to chemical adhesion.

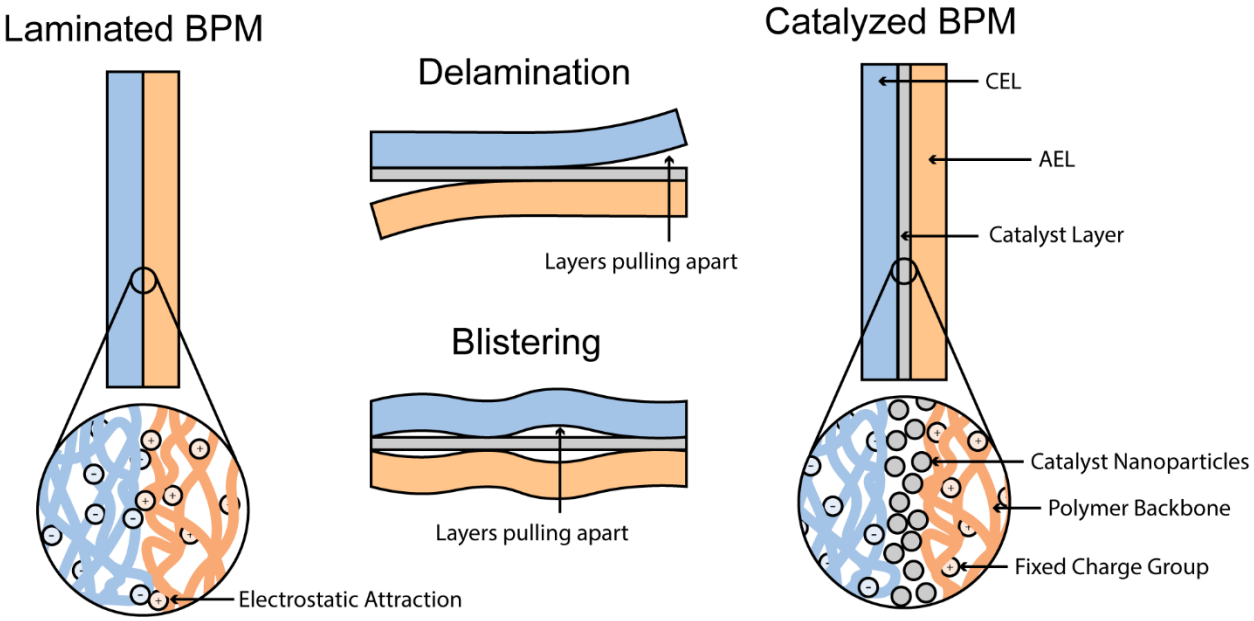

Figure 4.2: Schematic depicting the electrostatic attraction in laminated BPMs, mechanisms of mechanical failure through delamination and blistering when the electrostatic attraction is interrupted, and the catalyst layer in catalyzed BPM that interrupts the electrostatic attraction between the CEL and AEL.

Results/Discussion

Inherent adhesion between laminated BPM layers

At this point in time, there is a vast range of AEM and CEM types to choose from when making the layers for a BPM.[11] These membranes differ in their basic construction, from backbone to functional group, but also differ in their manufacturing techniques, durability, and applications.

This leads to the membranes having dramatically different permselectivity, conductivity, and surface energy. Presently, it would be short-sighted to eliminate certain membranes based on specific parameters, as the connection between these parameters is not well understood, and a membrane built for one application might serve well in an unintended application. To explore different possible membrane combinations, we did a series of T-peel to examine the inherent adhesion between different commercially available AEMs/CEMs (Figure 4.3).

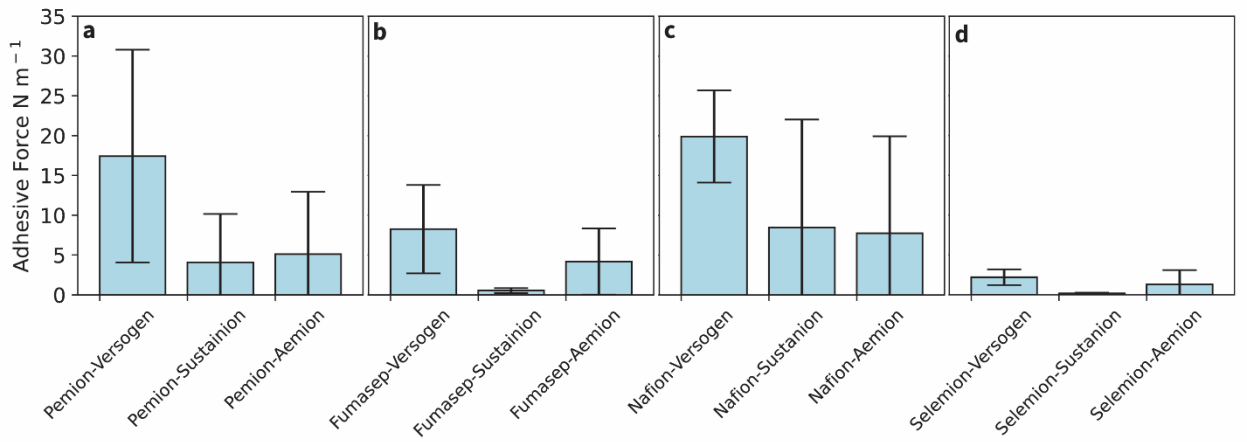

Figure 4.3: Adhesive forces, determined using T-peel, between anion- and cation-exchange membranes that were laminated together and mildly pressed while hydrated.

From Figure 4.3, it is obvious that not all commercial CEM and AEM combinations are created equal. While Selemion and Fumasep CEMs perform well in other categories, they seem to have lower inherent adhesive force than alternatives like Nafion and Pemion. Furthermore, Versogen AEMs seem to consistently have higher adhesion than Sustanion and Aemion membranes. The potential root cause of these differences could be the orientation or type of functional group in the respective AEM and CEM. These functional groups can allow for an electrostatic attraction between the two BPM layers. With differences in membrane composition and manufacturing, these functional groups may lead to different synergistic relationships when laminated together. To investigate this relationship, a CEM was cast onto differently charged backing materials. The surface energy of the backing materials would either encourage the orientation of functional groups toward the backing material, or orient the polymer backbone toward the backing material. For example, if the backing material encouraged the functional groups to orient toward the surface, when that CEM is then layered with the AEM, the AEM will now have a larger number of functional groups to form electrostatic interactions with.

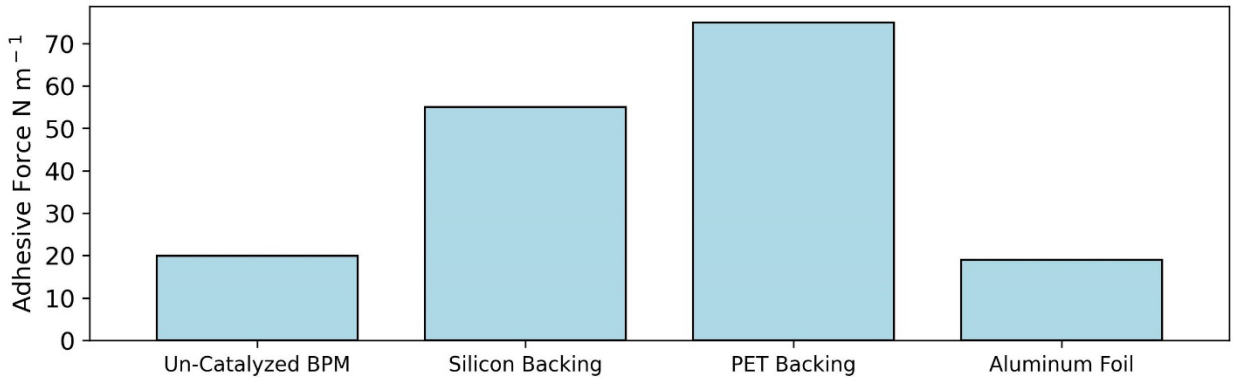

Figure 4.4: Adhesive forces, determined using T-peel, between anion- and cation-exchange membranes that were laminated together and mildly pressed while hydrated. The anion-exchange membrane was Versogen, while the cation-exchange membrane was a cast SPEEK polymer. The backing material over which the SPEEK polymer was cast is varied.

From Figure 4.4, it is obvious that when adhering the uncatalyzed BPM layer together, the backing material used when casting the CEM impacts the adhesion at the BPM junction. The electrostatic interactions between the functional groups at the BPM junction assist in adhering the BPM layers together. However, all the adhesive forces between the laminated AEM and CEMs are fairly weak. For reference, Scotch tape has an adhesive force of around 120 N m^{-1}. These laminated membranes will not hold up to high current applications, as the layers would delaminate and lead to pockets of water at the BPM junction.[66, 78] Adhesion could be introduced chemically or through physical interlocking of the polymers to address the issues seen with laminated BPM layers.

Introducing chemical adhesives

The adhesion mechanisms that take advantage of chemical/intermolecular interactions are known as specific adhesion mechanisms. Specific adhesion mechanisms involve intermolecular interactions, such as Van der Waals, electrostatic gradients, hydrogen-bonding, etc.[79] For an application like adhering the layers of the BPM together, specific adhesion mechanisms are likely the least disruptive mechanism. Specific adhesion could be introduced through compatible hydrogels, leading to minimal impact on the transport of water and ionic species, as the hydrophilic domains are maintained at the junction.[80] Specific adhesion might also be introduced through the introduction of molecules that can preferentially form electrostatic connections between the AEM

and CEM functional groups, or through in introduction of catalysts that have intermolecular forces, such as pi-pi interactions.

To explore the introduction of specific adhesion mechanisms, a suite of different hydrogels were investigated, including the introduction of an ion-exchange ionomer to the BPM junction. To best understand the impact of these adhesives, these hydrogels were combined with different water dissociation catalysts and thus the adhesive values can be compared to catalyzed Nafion-Versogen BPMs, which have good electrochemical performance. The hydrogels chosen had either already shown precedent for adhesion with at least one half of the BPM, the AEM or the CEM, or has shown proficiency for ion conduction.

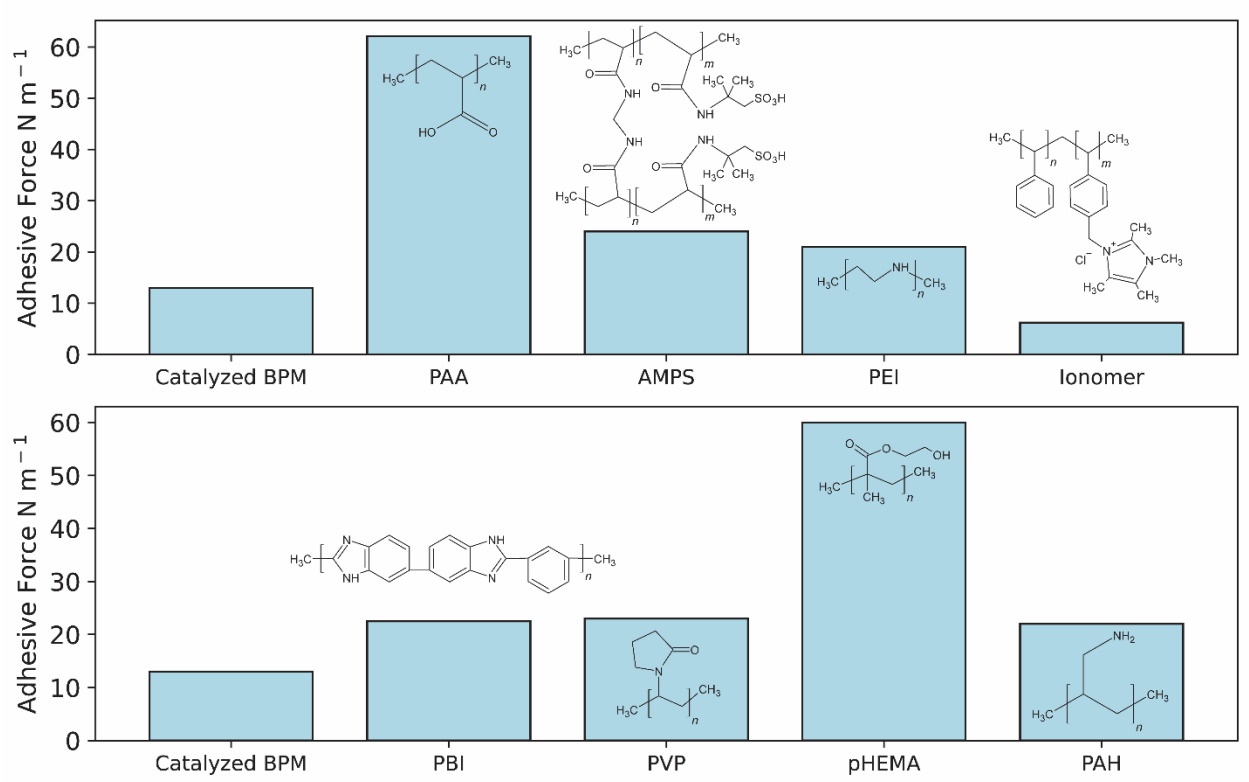

Figure 4.5: Adhesive forces, determined using T-peel, comparing a catalyzed Nafion-Versogen BPM to catalyzed Nafion-Versogen BPM with introduced hydrogels. The hydrogels considered are poly(acrylic acid) (PAA), 2-acrylamido-2-methylpropane sulfonic acid based (AMPS), poly(ethylenimine) (PEI), Sustainion ionomer (Ionomer), poly(benzmidazole) (PBI), poly(vinylpyrrolidone) (PVP), poly(2-hydroxyethyl methacrylate) (pHEMA), and poly(allylamine) (PAH).

From Figure 4.5, the only introduced hydrogel that did not provide increased adhesion was the introduction of an ionomer, specifically Sustainion ionomer. Sustainion is an anion-exchange ionomer, and with the introduction of this ionomer the adhesive forces between the AEM and CEM would likely take on the characteristics of a pristine Nafion-Sustainion BPM. As seen in Figure 4.3, the adhesion between the Nafion-Sustainion BPM is less than that of the Nafion-Versogen BPM, and the resulting adhesive forces were within the range observed for the pristine Nafion-Sustainion BPM. Ideally, an ionomer like Versogen would have been much preferred, but high concentration ionomer solutions of commercially available ionomers are not always available.

To attempt to utilize the electrostatic interactions between the CEM's negatively charged groups and potentially positively charged groups on a hydrogel, polymers with nitrogen groups were investigated. These hydrogels included poly(ethylenimine) (PEI), poly(benzmidazole) (PBI), and poly(allylamine) (PAH). Interestingly, these three hydrogels showed similar adhesive forces, but did not present adhesive forces strong enough to be worth introducing to the BPM junction.

Alternatively, the interactions between negatively charged groups, like carboxylates, electrostatically attracted to the positive stationary groups on the AEM, were also considered. For this group, the hydrogels considered were poly(vinylpyrrolidone) (PVP), poly(2-hydroxyethyl methacrylate) (pHEMA), and poly(acrylic acid) (PAA). Both pHEMA and PAA showed an increase in the adhesive forces between Nafion and Versogen, while PVP only showed a marginal increase in adhesive force (Figure 4.5).

The remaining hydrogel tested was 2-acrylamido-2-methylpropane sulfonic acid based (AMPS), that sports sulfonic acid groups that were expected to bond well to the stationary positive groups on the AEM. Furthermore, AMPS was previously used by Nemati et al. to introduce ion conductivity to a membrane surface.[81] With the AMPS hydrogel, there was also the introduction of possible crosslinking, which is used to improve the tensile strength/mechanical durability of hydrogels.[82-84] The introduction of crosslinking might help with preventing the hydrogel tensile strength from being the weakest link in the BPM structure, but poor adhesion was found between the AMPS hydrogel and the CEM and AEM polymers, leading to essentially a third layer at the BPM junction.

The issue of hydrogel adhesion to the CEM and AEM polymers was a consistent issue seen for most of the hydrogel explore. To move past the issue of forming a third polymer layer at the

BPM junction, the introduction of molecules that could bridge the AEM and CEM were explored. These molecules include water dissociation catalysts that could form at the junction and introduce binding mechanisms like pi-pi stacking or hydrogen bonding. Other molecules explored utilized the basic mechanisms found in nature or in industrial glues, like silane interactions or catechol interactions.[85-88]

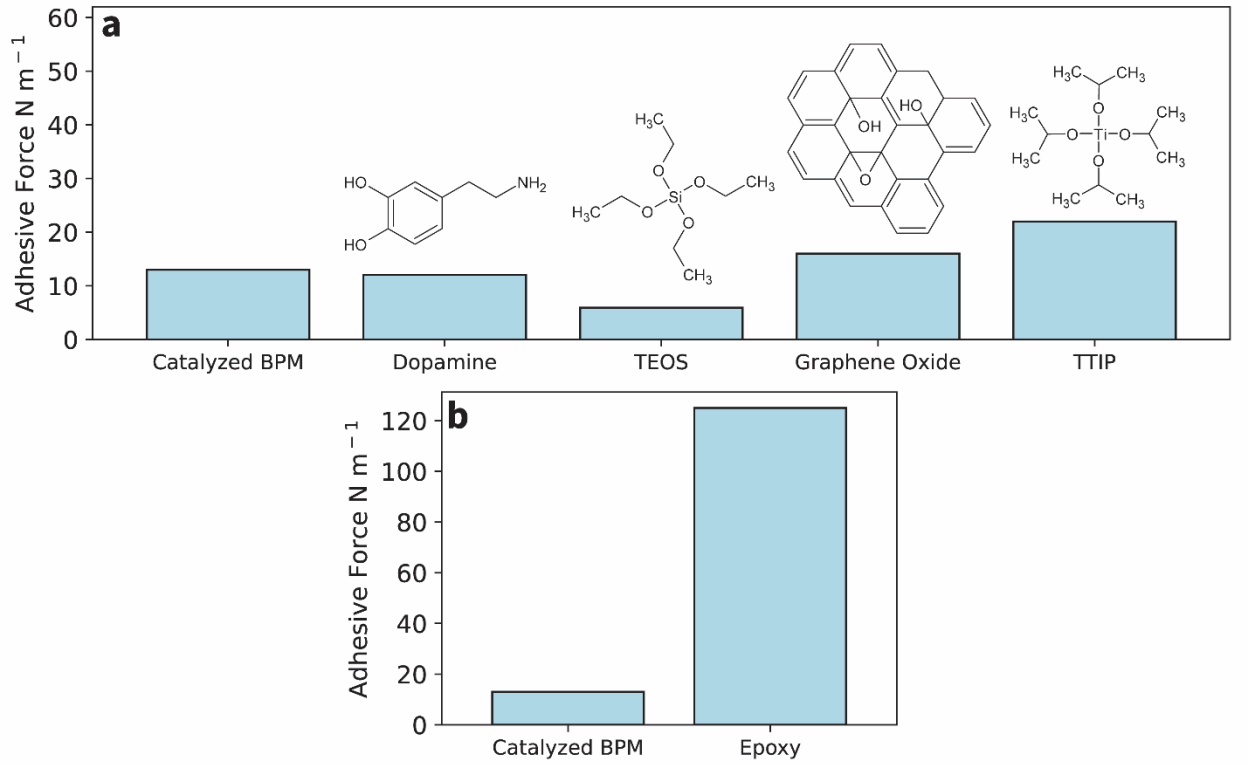

Figure 4.6: (a) Adhesive forces, determined using T-peel, comparing a catalyzed Nafion-Versogen BPM to catalyzed Nafion-Versogen BPM with introduced intermolecular adhesives like dopamine, and silane interactions, like tetraethyl orthosilicate (TEOS) and commercial epoxy. (b) Adhesive forces, determined using T-peel, comparing Nafion-Versogen BPM catalyzed with water dissociation catalysts to Nafion-Versogen BPM catalyzed with adhesion inducing catalysts such as graphene oxide and titanium isopropoxide (TTIP).

The introduction of graphene oxide, used commonly as a water dissociation catalyst, presented no notable improvement in adhesion between the CEM and AEM layers of the BPM (Figure 4.6a).[50, 89, 90] It was expected that the introduced aromatic rings would allow for pi-cation or pi-anion interactions between the catalyst and the AEM, or the CEM.[91-95] Furthermore, there was only a marginal increase in adhesion when the titanium isopropoxide (TTIP) was introduced

to the junction. For this catalyst, the idea was to introduce a precursor that would convert into a water dissociation catalyst at the BPM junction.

The introduction of dopamine was inspired by the adhesives used by marine tunicates and other marine invertebrates.[96, 97] In hydrated environments, the catechol of dopamine are able to form strong hydrogen bonds, while also presenting a means to crosslink polymers together.[85, 98, 99] However, in the application of binding AEM and CEM together at the BPM junction, dopamine was unable to achieve high enough adhesion to be significant. The dopamine additive may be a good adhesive for medical applications, but the adhesive forces required for BPM are too high.

To explore a more nuclear option, the root mechanism for a large number of industrial adhesives was explored. With the introduction of silanes, the mechanisms of carbon-silicon covalent bonds and alkoxy groups reacting with hydroxyl groups can be used to adhere materials together.[100] This is a common adhesion mechanism for hydrated environments and is used for binding hydrogels in the medical industry and in microfluidics.[101-103] However, the introduction of tetraethyl orthosilicate (TEOS) showed little improvement to the AEM and CEM adhesion at the BPM junction. This lack of interaction may have been due to the surface of Nafion being deficient in hydroxyl groups for binding, or perhaps a byproduct of the chemically stable fluorinated structure of Nafion itself. The final resort was to consider a two-part epoxy used in marine application, to demonstrate that the AEM and CEM of the BPM can be held together chemically. Figure 4.6b shows that the introduction of even a small amount of industrial grade epoxy can finally adhere the BPM layer together. However, the performance of the epoxy containing BPM was terrible, and likely an epoxy is not the answer to adhering BPM layers together.

With the range of hydrogels and introduced compounds explored, there still remains even more untested or unexplored. For example, varying the crosslinking or molecular weight of the introduced hydrogel may hold the secret to adhering the BPM layers.[104] Additionally, a cleaver functionalization of the water dissociation catalyst surface might also present a viable avenue for introducing adhesion to the BPM junction.[89] However, all the methods tested still provide only marginal increases in adhesion between the BPM layers of a catalyzed BPM. As a reminder, Scotch tape has an adhesive force of 120 N m^{-1}, while the best performing hydrogel could only yield an adhesive force of ~ 60 N m^{-1}. This could be due to the limited tensile strength of the hydrogels tested and might be overcome by cross-linking. The interactions of specific adhesion

mechanisms (e.g. Van der Waals interactions, electrostatic gradients, hydrogen-bonding) can be strong when in high concentration, however this may lead to drastic changes in the hydrogel characterizations and interaction with the membrane it adheres to, defeating the purpose of utilizing hydrogels for this application by potentially impeding the transport of water and ions through the junction. Furthermore, specific adhesion mechanisms require thorough contact between the two substances making up the adhered assembly, as these adhesion mechanisms can only form an adhesion boundary of ~10^{-7}-10^{-3} mm thick, thus the material's roughness/contact cannot exceed this boundary distance.[79] Beyond this, due to the importance of good contact when forming a specific adhesion assembly, contaminants become an increasingly important issue as the boundary layer decreases and interrupts the adhesion mechanism, here this 'contaminant' can be the water dissociation catalyst itself. Alternative adhesive mechanisms to consider are those that utilize mechanical adhesion mechanisms, such as increased surface area and physical interlock.

Utilizing physical interlocking of BPM layers

Mechanical adhesion is the physical interlocking of materials to form an adhesive bond, for example like the utilization of wood glues that will harden in the vesicles of dead wood, locking the glue and the wood together. Mechanical adhesion is able to form much larger boundary layers of ~10^{-4}-1 mm and are thus less impacted by the roughness of the surfaces being adhered (Figure 4.7). Additionally, because mechanical adhesion does not rely strictly on manipulating the surface energy of the assembled materials, it is less likely to be impacted by small 'contaminants' such as water dissociation catalysts, mitigating the concerns for contamination.

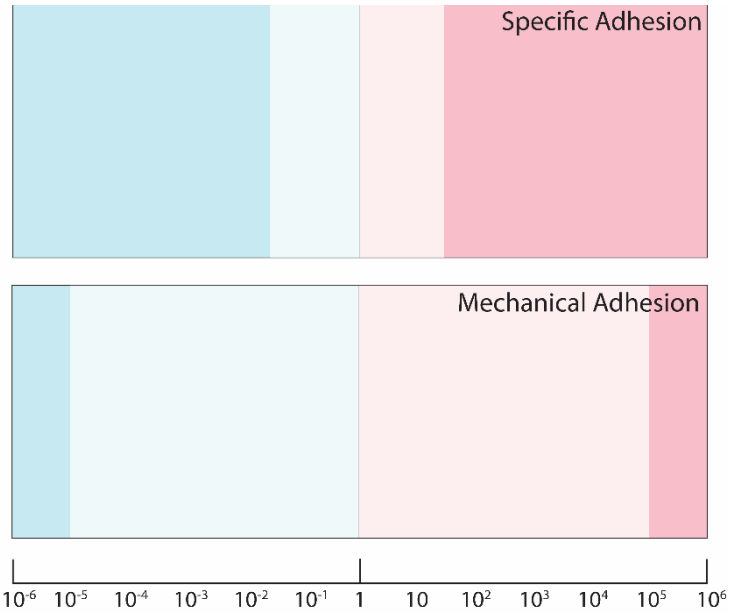

Figure 4.7: Boundary layer thickness in mm (white) comparison between specific adhesion mechanisms and mechanical adhesion mechanisms.

To begin exploring the utilization of mechanical adhesion at the BPM junction, the manipulation of the polymer structure of the AEM and CEM was explored. Heat pressing is a common method sited for forming BPM.[105, 106] This method is thought to expand the polymer and introduce polymer backbone mobility. Allowing for the two layers to integrate their polymer backbones and lead to a mechanical interlock between the polymers when the membrane is cooled. To explore this mechanism, a series of BPM were heated in different water bath temperatures while being pressed together by metal plates.

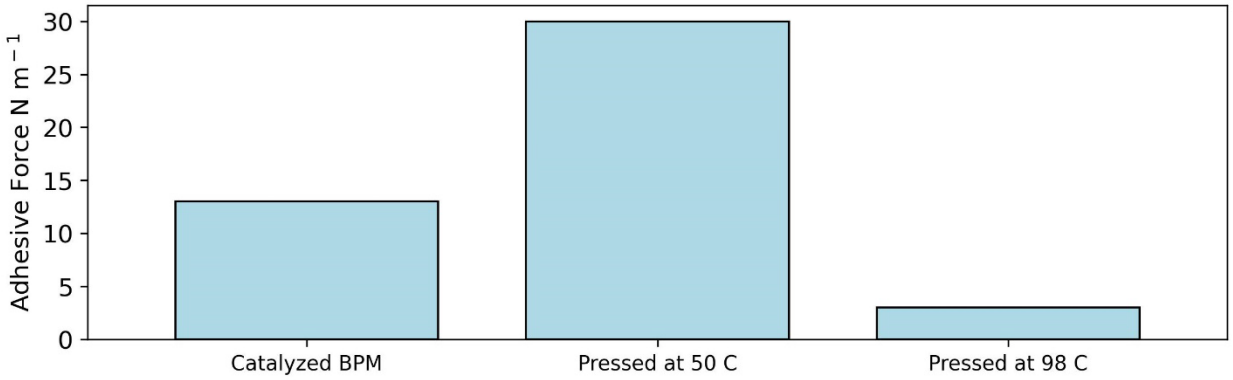

Figure 4.8: Adhesive forces, determined using T-peel, between anion- and cation-exchange membranes that were laminated together and mildly pressed for 1 hour while hydrated at varied temperatures.

Interestingly, there are diminishing returns as temperature is increased beyond 50 °C (Figure 4.8). The likely cause of reduced adhesion at elevated temperatures is excessive swelling of the BPM polymers, leading to poor tensile strength of the polymer, or an embrittlement of the ionomer as temperature is increased for pressing and then brought down to room temperature for T-peel testing.[107] The embrittlement of the ionomer stems from the counter-ion used to stabilize the structure during storage or heating. For example, for long term storage in dry conditions, AEMs are often exchange with larger anionic groups, like iodide or even carbonate.[108, 109] Overall this experiment shows that the polymers can be moved and used to induce adhesion at the BPM junction.

To encourage more entanglement between the polymeric backbones of the AEM and CEM, solvent can be utilized to swell the polymer, leaving room for the backbones to migrate and integrate at elevated oven temperatures. For the solvent used to swell the polymer, it is a balance between swelling and completely dissolving the polymer. Additionally, the AEM and CEM polymers will swell differently due to differences in parameters like the ion-exchange capacity and varied backbone chemistries.[12] Thus, simply introducing a solvent to the BPM junction will lead to a wrinkled BPM junction. To overcome this, one of the BPM layers can be cast over the other, taking advantage of the cast solvent to swell the already formed membrane being cast over. For this, a sulfonated poly(ether ether ketone) (SPEEK) CEM was dispersed in solvent and cast over a Versogen AEM. With this we see the formation of a mixed layer, where the mobile chains in the cast CEM integrate into the swollen backbone of the AEM (Figure 4.9).

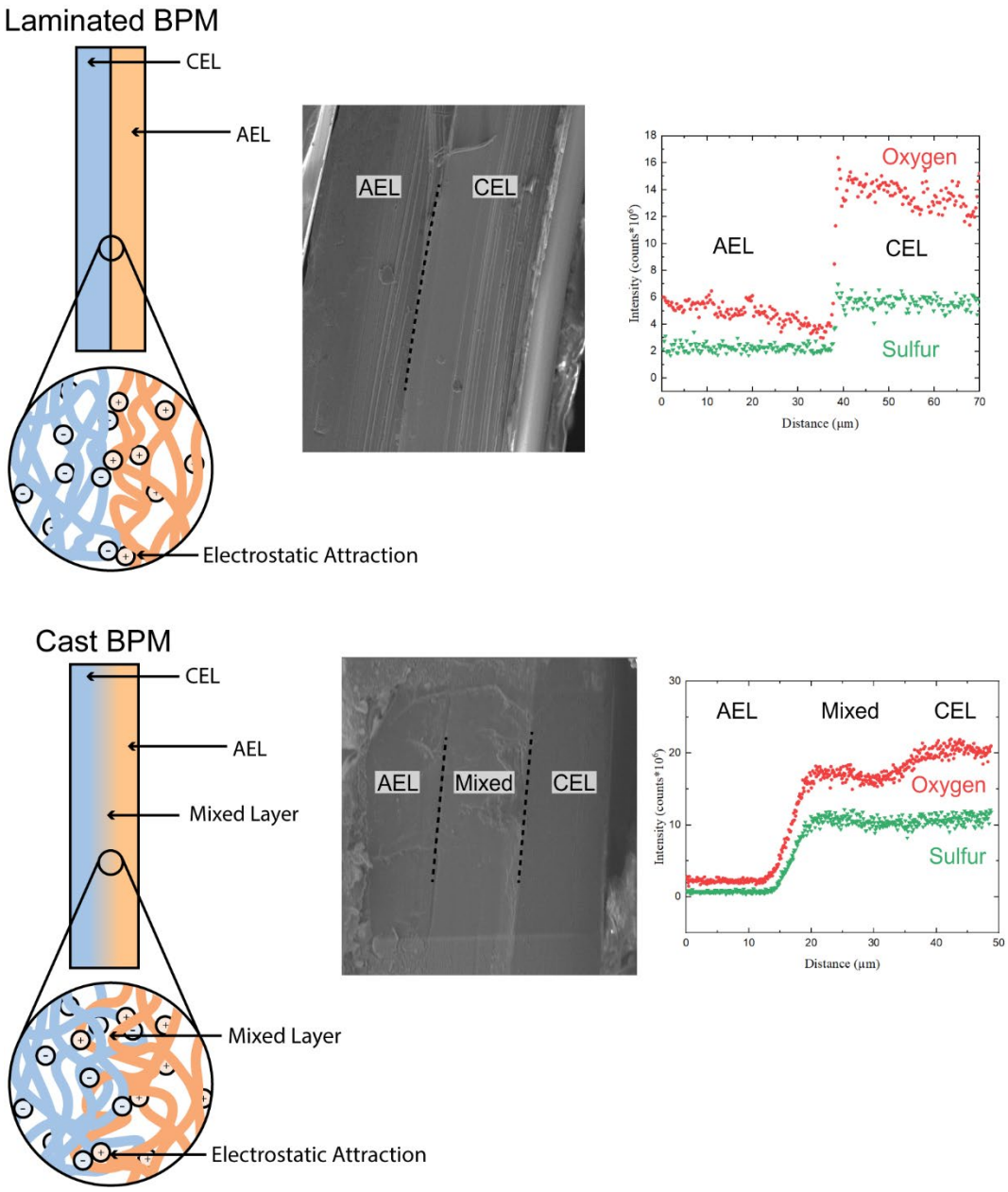

Figure 4.9: SEM and TOF-SIM methods were used to compare the laminated BPM to the cast BPM. Revealing a mixed layer in the cast BPM, that can not be found in the laminated BPM.

The method of fully integrating the backbones of the AEM and CEM together has led to essentially the formation of one solid BPM. With this physical interlock of the polymer backbones, the adhesion between the CEM and AEM is very high (Figure 4.10).

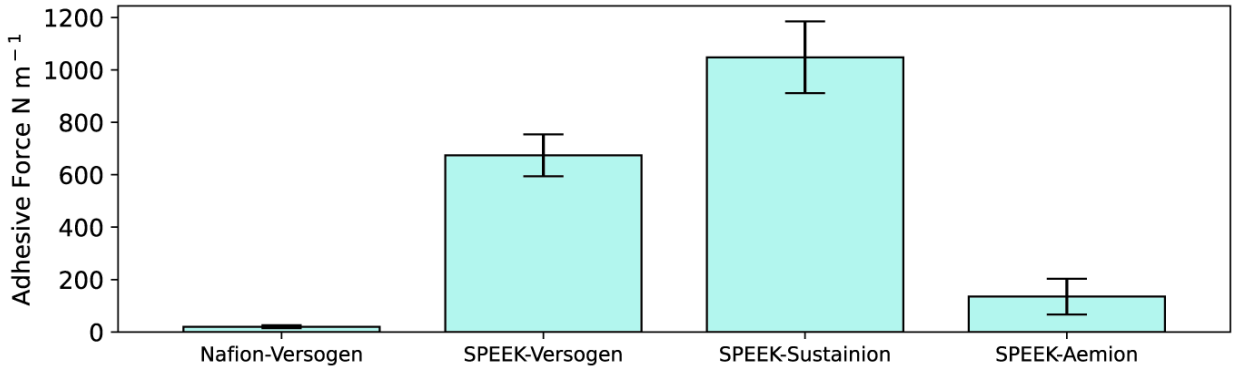

Figure 4.10: Adhesion values for cast CEM over various AEMs compared to laminated an uncatalyzed Nafion-Versogen BPM.

With the formation of a mechanically robust BPM, the parameters controlling the migration of the CEM polymer and swelling of the AEM polymer were explored. Factors that could impact CEM polymer migration include the molecular weight, or chain length, of the CEM polymer as well as the time allowed for the polymer to migrate at elevated temperatures.[110]

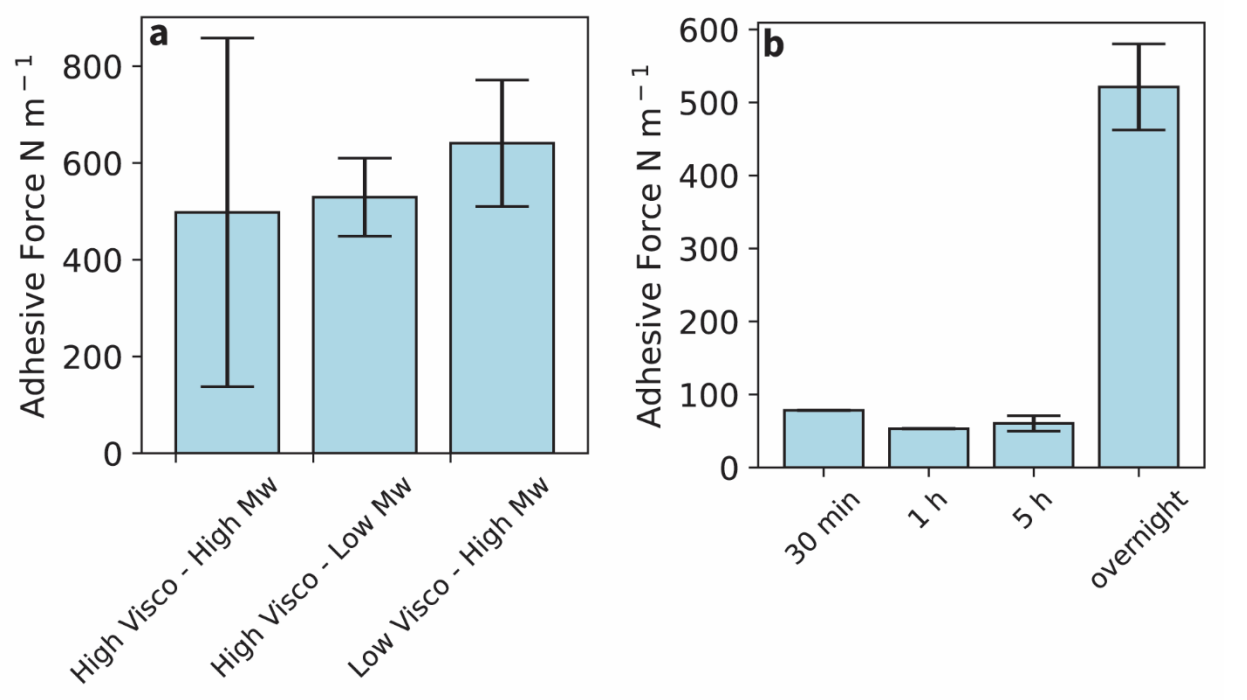

Figure 4.11: (a) Adhesion values for varied CEM cast solution viscosity and molecular weight cast over Versogen AEM. (b) Adhesion values for varied oven time for setting the cast CEM over the Versogen AEM.

From Figure 4.11, the impact of viscosity and molecular weight are not immediately obvious. Further work needs to be conducted to explore a wider range of CEM polymer molecular weights, as the range explored was likely not large enough to capture the trend, as the data suggests there is no correlation between molecular weight and BPM adhesion. Additionally, the setting time in the oven needs to be explored between the 5 hour and overnight span (Figure 4.11b). Further testing looking at the adhesion at 8 hours and 16 hours would greatly improve our understanding of how the mixed layer at the BPM junction is formed. However, it is still clear that if the polymer is not given sufficient time to form this mixed layer, the BPM adhesion suffers. To explore the differential parameters of the AEM that might impact polymer mixing, the counter-ions in the AEM were exchanged for varying anions.

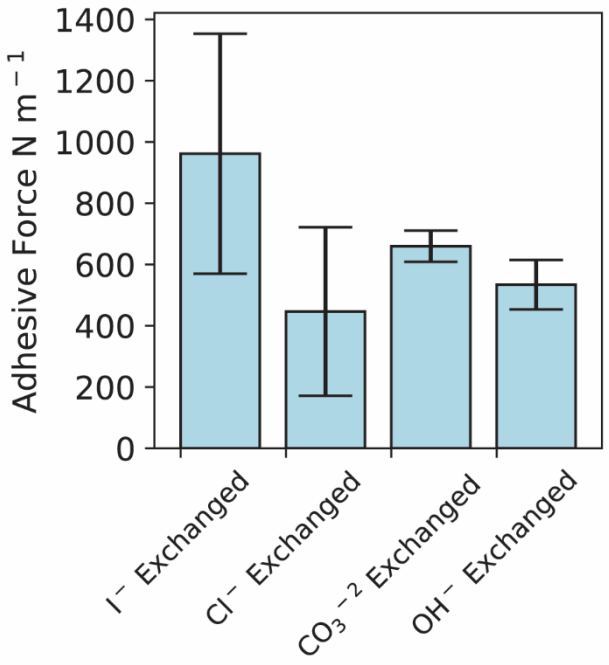

Figure 4.12: Adhesion values for cast CEM over ion-exchange Versogen. The anions exchanged into the AEM include iodide (I^-), chloride (Cl^-), carbonate (CO_3^{2-}), and hydroxide (OH^-).

Figure 4.12 indicates that the introduction of a large anion, like iodide, might allow for increased swelling of the AEM and thus further integration of the cast CEM into the AEM, but the error for these BPM is large. Overall, it appears that the swelling difference when exchanging the counter-ion of the AEM, is not significant enough to impact the formation of the BPM mixed layer. Further

studies could explore the change in mixed layer thickness through SEM or TOF-SIMS data, while also exploring elevated setting temperatures, as the iodide exchanged AEM, for example, will be less brittle at elevated temperatures.

With the improvements in BPM layer adhesion, the introduction of catalyst to the BPM junction is the next important step toward solving the adhesion issue in advanced catalyzed BPM. When adding catalyst to the BPM junction, adhesive forces are overall still much higher than simply laminating the AEM and CEM layers together (Figure 4.13).

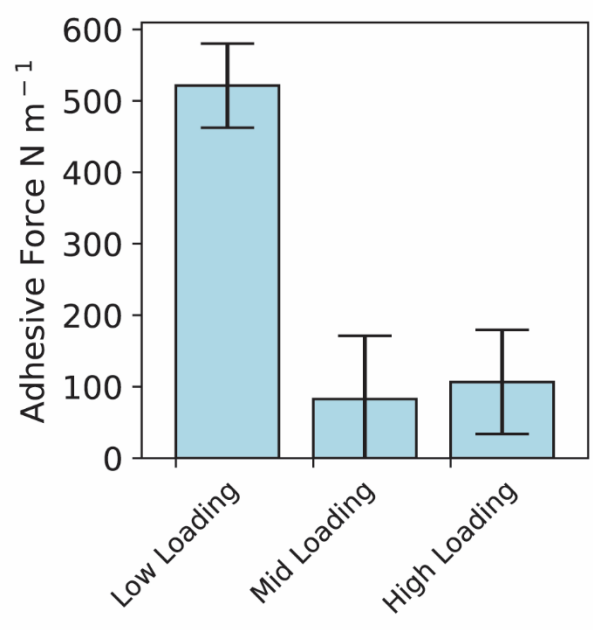

Figure 4.13: Adhesion values for cast CEM over Versogen with varied catalyst loading at the BPM junction.

However, as more catalyst is added to the BPM junction the adhesion between the AEM and CEM decreases. This is likely due to a thicker catalyst layer blocking the migration of the cast CEM toward the AEM, or the CEM reaching the limit to its travel length and unable to traverse the entire catalyst layer before the solvent is cooked off during the setting process. This trend could be further explored by varying the oven temperature of a high loading BPM, or by changing the solvent to CEM polymer ratio, leaving more time for the CEM to migrate while the solvent is baking off.

Conclusions

Introducing chemical adhesives requires good adhesive forces between the adhesive and both the AEM and the CEM. With the differences in polymer charges and construction, this is not a trivial hurtle. Additionally, the introduced adhesive needs good mechanical and tensile strength, while also not impeding ion transport at the BPM junction, where transport is the most critical. Utilizing physical interlocking at the BPM junction is likely the best option, however this can also lead to potentially damaging the membrane layers during pretreatment as this introduces partial dissolution of one or more membrane layer. The most promising option is to cast at least one of the polymer layers, allowing for a mixed layer to form and physically tie the BPM layer together. Unfortunately, the casting method is still impacted by the introduction of catalyst to the BPM junction. The catalyst at the BPM junction is critical to meet BPM performance goals required by the high current applications that would utilize these BPM and must be integrated into the BPM junction.

Experimental Methods

Exchanging counter-ions in AEM samples:

The Versogen membrane purchased from Fuel Cell Store as 40 micron, self-supported PiperION is shipped in a carbonate form, meaning that the counter-ion to the quaternary amine groups fixed to the polymer backbone are carbonate anions. To prepare the different ion-exchange forms of Versogen, the membranes were soaked in concentrated salt solutions containing the desired anion to be exchanged into the AEM.

For the carbonate containing samples, the Versogen was taken from the packaging and hydrated in DI H_2O. The DI H_2O was allowed to exchange for 6 hours and was then replaced with fresh DI H_2O and allowed to soak for at least 24 hours.

For the chloride and iodide containing samples, the Versogen samples were soaked in a solution of 1 M NaCl and 1 M NaI, respectively. The samples were placed in a 60 ^{o}C oven to help facilitate the exchange of the membrane, and the soaking solution was exchanged for fresh salt solutions three times a day for three days. There were no visible changes to the chloride containing Versogen samples, but the iodide samples took on a vibrant yellow color.

For the hydroxide exchanged Versogen, the typical conditioning procedure provided by Versogen was followed. The Versogen was soaked in 0.5 M KOH for 6 hours and then exchange for fresh solution, then left to soak for at least another 24 hours before using.

Preparation of CEM cast solutions:

CEM cast solutions started as SPEEK powder provided by a collaborator. The SPEEK powder was combined with dimethylacetamide (DMAc) to achieve a weight percent of SPEEK to solvent in the range of 20-30 wt%. The powder and the DMAc were combined in glass containers that were sealed with parafilm and covered with aluminum foil to prevent potential UV degradation of the polymer. The solution was left on a rocker table set to 70 rpm for at least 24 hours, or until there were no visible swirls or bubbles in the SPEEK solution.

Collecting and analyzing T-peel data:

T-peel data was collected using two different membrane preparation techniques, depending on the predicted degree of adhesion between the AEM and CEM layers of the BPM. For BPM with predicably low adhesion (<100 N m^{-1}), one membrane layer was placed on a glass slide, with a piece of 0.0005" thick PET placed at one end, blocking a section that will later be used as a tab to clamp the T-peel instrument to. Then the opposite membrane layer is pressed onto the other membrane layer and a second glass slides is placed on top to form a sandwich. A clip was used to hold the membrane layers together while inserting the BPM into the T-peel instrument, leaving a 1 cm long tab for clamping on both BPM layers. These tabs are clamped into either side of the T-peel instrument in an orientation that allows the BPM layers to be pulled apart (Figure 4.14).

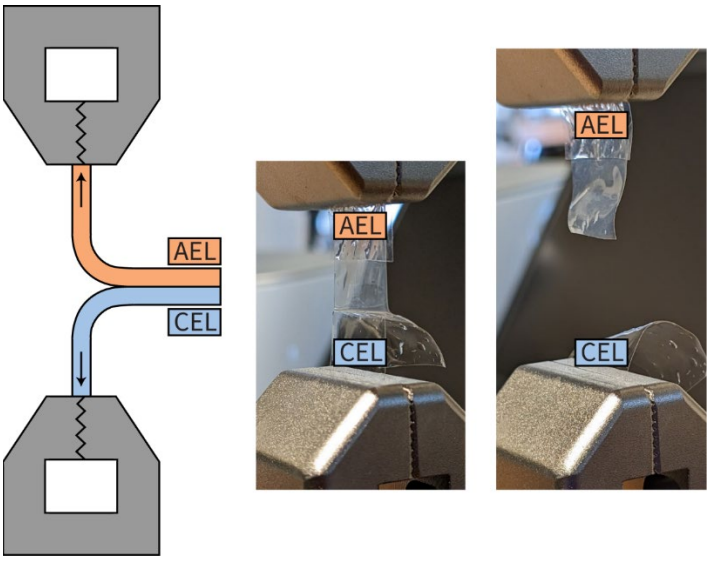

Figure 4.14: Schematic showing the BPM layers clamped to the T-peel instrument.

The membranes are pulled apart at a rate of 20 mm min^{-1}, with a newton meter recording the force required to pull the layers apart.

For BPM with a predicted adhesion force >100 N m^{-1}, special BPM preparation is required, as this adhesive force exceeds the tensile strength of most membranes being considered. For these membranes, a small strip of exposed AEM, or CEM, is masked off using 0.0005" thick PET film, leaving a gap of about 5 mm down the length of the BPM and a 1 cm tab at the top to initiate the peel from (Figure 4.15).

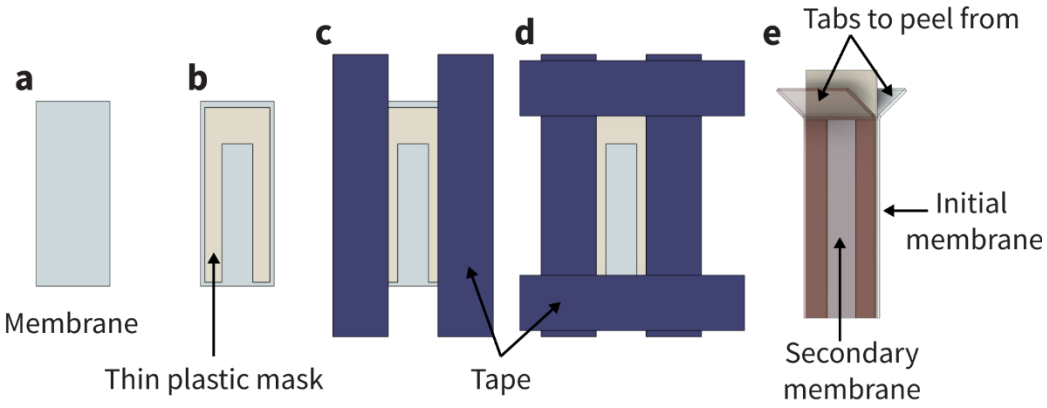

Figure 4.15: Schematic showing the steps to preparing a bipolar membrane, with a predicted adhesion >100 N m^{-1}, for T-peel testing. Going through the introduction of a thin plastic mask (b) that prevents adhesion between the two bipolar membrane layers, to the final resulting bipolar membrane where the membrane has two tabs constructed from the membrane layers that can be peeled apart (e).

Then the other membrane layer is pressed or cast on, forming the BPM. To this prepped BPM, waterproof white Flex Tape is cut into 6 mm strips and adhered to either side of the BPM. These tape strips are then clamped into either side of the T-peel instrument and pulled apart at a rate of 20 mm min^{-1}. This method allows the tensile strength of the membrane layers to no longer limit the forces measured, producing an adhesion value that is closer to the true value of adhesion between the BPM layers.

To analyze the resulting T-peel data, an average is taken of the plateau region of the T-peel (Figure 4.16). A typical T-peel measurement will have a spike at the initiation of the peel, then a plateau until the end of the membrane is reached. Each peel was collected in triplicated (at least), allowing the inclusion of error bars in the bar plots comparing BPM adhesion.

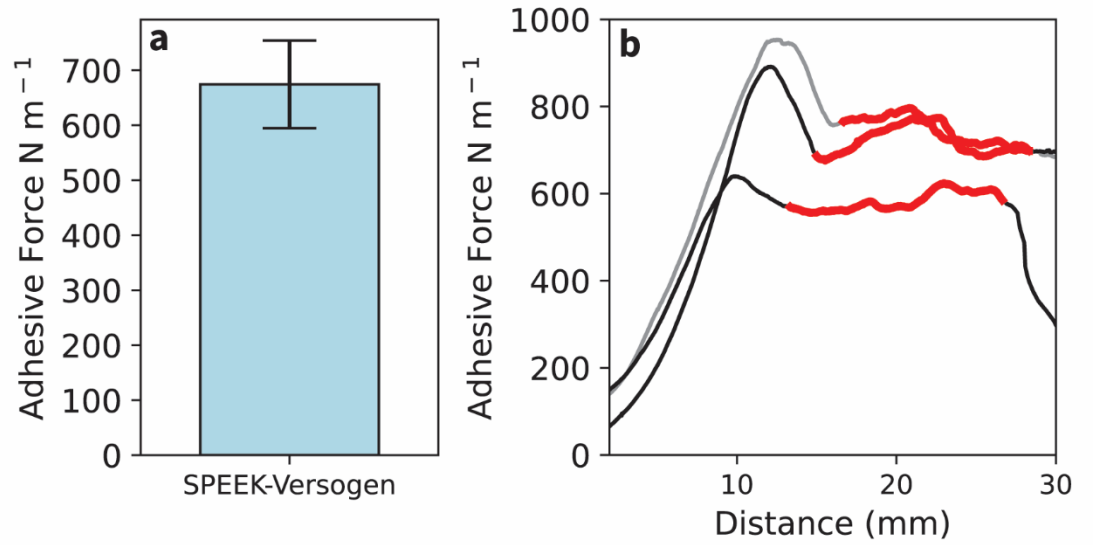

Figure 4.16: Triplicates of one BPM, showing the initial spike and then the averaging of the plateau region used for making the bar chart of the adhesive values.

REFERENCES CITED

1. Boretti, A.; Rosa, L. Reassessing the projections of the World Water Development Report. *npj Clean Water* **2019**, *2* (1). DOI: 10.1038/s41545-019-0039-9.

2. Gates, B. *How to avoid a climate disaster*; Allen Lane, 2025.

3. Thiel, G. P.; Stark, A. K. To decarbonize industry, we must decarbonize heat. *Joule* **2021**, *5* (3), 531-550. DOI: https://doi.org/10.1016/j.joule.2020.12.007.

4. Friedlingstein, P.; O'Sullivan, M.; Jones, M. W.; Andrew, R. M.; Bakker, D. C. E.; Hauck, J.; Landschützer, P.; Le Quéré, C.; Luijkx, I. T.; Peters, G. P.; et al. Global Carbon Budget 2023. *Earth Syst. Sci. Data* **2023**, *15* (12), 5301-5369. DOI: 10.5194/essd-15-5301-2023.

5. Mowbray, B. A. W.; Zhang, Z. B.; Parkyn, C. T. E.; Berlinguette, C. P. Electrochemical Cement Clinker Precursor Production at Low Voltages. *ACS Energy Lett.* **2023**, *8* (4), 1772-1778. DOI: 10.1021/acsenergylett.3c00242.

6. Stocker, T. F.; D. Qin; G.-K. Plattner; M. Tignor; S.K. Allen; J. Boschung; A. Nauels; Y. Xia; V. Bex; Midgley, P. M. *Climate Change 2013: The Physical Science Basis. Contribution of Working Group I to the Fifth Assessment Report of the Intergovernmental Panel on Climate Change*; Cambridge University Press, 2013.

7. Sasmal, S.; Chen, L.; Sarma, P.; Traenkle, O. P.; Simons, C. R.; Wells, K. M.; Spontak, R. J.; Boettcher, S. W. Water-dissociation catalysis near the reversible limit in bipolar membrane electrolyzers. *Nat. Mater.* **2024**.

8. Bui, J. C.; Lees, E. W.; Marin, D. H.; Stovall, T. N.; Chen, L.; Kusoglu, A.; Nielander, A. C.; Jaramillo, T. F.; Boettcher, S. W.; Bell, A. T.; et al. Multi-scale physics of bipolar membranes in electrochemical processes. *Nature Chemical Engineering* **2024**, *1* (1), 45-60. DOI: 10.1038/s44286-023-00009-x.

9. Campione, A.; Gurreri, L.; Ciofalo, M.; Micale, G.; Tamburini, A.; Cipollina, A. Electrodialysis for water desalination: A critical assessment of recent developments on process fundamentals, models and applications. *Desalination* **2018**, *434*, 121-160. DOI: 10.1016/j.desal.2017.12.044.

10. Gurreri, L.; Tamburini, A.; Cipollina, A.; Micale, G. Electrodialysis applications in wastewater treatment for environmental protection and resources recovery: A systematic review on progress and perspectives. *Membranes (Basel)* **2020**, *10* (7). DOI: 10.3390/membranes10070146 From NLM PubMed-not-MEDLINE.

11. Espinoza, C.; Kitto, D.; Kamcev, J. Counter-ion conductivity and selectivity trade-off for commercial ion-exchange membranes at high salinities. *ACS Applied Polymer Materials* **2023**. DOI: 10.1021/acsapm.3c02102.

12. Ul Hassan, N.; Mandal, M.; Huang, G.; Firouzjaie, H. A.; Kohl, P. A.; Mustain, W. E. Achieving High-Performance and 2000 h Stability in Anion Exchange Membrane Fuel Cells by Manipulating Ionomer Properties and Electrode Optimization. *Adv. Energy Mater.* **2020**, *10* (40), 2001986. DOI: https://doi.org/10.1002/aenm.202001986 (acccessed 2025/04/09).

13. *CRC Handbook of Chemistry and Physics*; CRC Press, 2014.

14. Kim, Y.; Walker, W. S.; Lawler, D. F. Competitive separation of di- vs. mono-valent cations in electrodialysis: effects of the boundary layer properties. *Water Res.* **2012**, *46* (7), 2042-2056. DOI: 10.1016/j.watres.2012.01.004 From NLM Medline.

15. Li, F.; Meindersma, W.; de Haan, A. B.; Reith, T. Novel spacers for mass transfer enhancement in membrane separations. *J. Membr. Sci.* **2005**, *253* (1-2), 1-12. DOI: 10.1016/j.memsci.2004.12.019.

16. Koutsou, C. P.; Yiantsios, S. G.; Karabelas, A. J. Direct numerical simulation of flow in spacer-filled channels: Effect of spacer geometrical characteristics. *J. Membr. Sci.* **2007**, *291* (1-2), 53-69. DOI: 10.1016/j.memsci.2006.12.032.

17. Taamneh, Y.; Bataineh, K. Improving the performance of direct contact membrane distillation utilizing spacer-filled channel. *Desalination* **2017**, *408*, 25-35. DOI: 10.1016/j.desal.2017.01.004.

18. Messalem, R.; Mirsky, Y.; Daltrophe, N.; Saveliev, G.; Kedem, O. Novel ion-exchange spacer for improving electrodialysis II. Coated spacer. *J. Membr. Sci.* **1998**, *138*, 171-180.

19. Kwon, K.; Park, B. H.; Kim, D. H.; Kim, D. Comparison of spacer-less and spacer-filled reverse electrodialysis. *Journal of Renewable and Sustainable Energy* **2017**, *9* (4). DOI: 10.1063/1.4996579.

20. Gurreri, L.; Tamburini, A.; Cipollina, A.; Micale, G.; Ciofalo, M. Flow and mass transfer in spacer-filled channels for reverse electrodialysis: a CFD parametrical study. *J. Membr. Sci.* **2016**, *497*, 300-317. DOI: 10.1016/j.memsci.2015.09.006.

21. Groisman, A.; Steinberg, V. Efficient mixing at low Reynolds numbers using polymer additives. *Nature (London)* **2001**, *410* (6831), 905-908. DOI: 10.1038/35073524.

22. Liashenko, I.; Hrynevich, A.; Dalton, P. D. Designing Outside the Box: Unlocking the Geometric Freedom of Melt Electrowriting using Microscale Layer Shifting. *Adv. Mater.* **2020**, *32* (28), 2001874. DOI: https://doi.org/10.1002/adma.202001874 (acccessed 2025/03/24).

23. Kim, J.; Bakirci, E.; O'Neill, K. L.; Hrynevich, A.; Dalton, P. D. Fiber Bridging during Melt Electrowriting of Poly(ε-Caprolactone) and the Influence of Fiber Diameter and Wall Height. *Macromol. Mater. Eng.* **2021**, *306* (3), 2000685. DOI: https://doi.org/10.1002/mame.202000685 (acccessed 2025/04/01).

24. Li, F.; Meindersma, W.; de Haan, A. B.; Reith, T. Experimental validation of CFD mass transfer simulations in flat channels with non-woven net spacers. *J. Membr. Sci.* **2004**, *232* (1-2), 19-30. DOI: 10.1016/j.memsci.2003.11.015.

25. Fimbres-Weihs, G. A.; Wiley, D. E. Review of 3D CFD modeling of flow and mass transfer in narrow spacer-filled channels in membrane modules. *Chemical Engineering and Processing: Process Intensification* **2010**, *49* (7), 759-781. DOI: 10.1016/j.cep.2010.01.007.

26. Fehér, J.; Keslerová, K.; Amrich, M. A tool for a spacer material and ion-exchange membrane compatibility evaluation for electrodialysis module design. *Periodica Polytechnica Chemical Engineering* **2018**, *62* (2), 144-149. DOI: 10.3311/PPch.10465.

27. Qian, X.; Anvari, A.; Hoek, E. M. V.; McCutcheon, J. R. Advancements in conventional and 3D printed feed spacers in membrane modules. *Desalination* **2023**, *556*, 116518. DOI: https://doi.org/10.1016/j.desal.2023.116518.

28. Bui, J. C.; Lees, E. W.; Marin, D.; Stovall, T. N.; Chen, L.; Kusoglu, A.; Nielander, A. C.; Jaramillo, T. F.; Boettcher, S. W.; Bell, A. T.; et al. Bipolar membrane fundamentals and applications in chemical processes. *Nature Chemical Engineering* **2023**.

29. Zhang, H.; Cheng, D.; Xiang, C.; Lin, M. Tuning the interfacial electrical field of bipolar membranes with temperature and electrolyte concentration for enhanced water dissociation. *ACS Sustainable Chemistry & Engineering* **2023**, *11* (21), 8044-8054. DOI: 10.1021/acssuschemeng.3c00142.

30. Pärnamäe, R.; Mareev, S.; Nikonenko, V.; Melnikov, S.; Sheldeshov, N.; Zabolotskii, V.; Hamelers, H. V. M.; Tedesco, M. Bipolar membranes: A review on principles, latest developments, and applications. *J. Membr. Sci.* **2021**, *617*. DOI: 10.1016/j.memsci.2020.118538.

31. Ge, Z.; Shehzad, M. A.; Yang, X.; Li, G.; Wang, H.; Yu, W.; Liang, X.; Ge, X.; Wu, L.; Xu, T. High-performance bipolar membrane for electrochemical water electrolysis. *J. Membr. Sci.* **2022**, *656*. DOI: 10.1016/j.memsci.2022.120660.

32. Giesbrecht, P. K.; Freund, M. S. Recent advances in bipolar membrane design and applications. *Chem. Mater.* **2020**, *32* (19), 8060-8090. DOI: 10.1021/acs.chemmater.0c02829.

33. Zhang, Y.; Yu, D.; Jia, C.; Sun, L.; Tong, A.; Wang, Y.; Wang, Y.; Huang, L.; Tang, J. Advances and promotion strategies of membrane-based methods for extracting lithium from brine. *Desalination* **2023**, *566*, 116891-116891. DOI: 10.1016/j.desal.2023.116891.

34. Yang, Y.; Gao, X.; Fan, A.; Fu, L.; Gao, C. An innovative beneficial reuse of seawater concentrate using bipolar membrane electrodialysis. *J. Membr. Sci.* **2014**, *449*, 119-126. DOI: 10.1016/j.memsci.2013.07.066.

35. Fernandez-Gonzalez, C.; Dominguez-Ramos, A.; Ibañez, R.; Irabien, A. Electrodialysis with bipolar membranes for valorization of brines. *Separation and purification reviews* **2016**, *45* (4), 275-287. DOI: 10.1080/15422119.2015.1128951.

36. Lim, A.; Kim, H.; Henkensmeier, D.; Jong Yoo, S.; Young Kim, J.; Young Lee, S.; Sung, Y.; Jang, J. H.; Park, H. S. A study on electrode fabrication and operation variables affecting the performance of anion exchange membrane water electrolysis. *Journal of Industrial and Engineering Chemistry* **2019**, *76*, 410-418. DOI: https://doi.org/10.1016/j.jiec.2019.04.007.

37. Mason, T. J.; Millichamp, J.; Neville, T. P.; Shearing, P. R.; Simons, S.; Brett, D. J. L. A study of the effect of water management and electrode flooding on the dimensional change of polymer electrolyte fuel cells. *J. Power Sources* **2013**, *242*, 70-77. DOI: https://doi.org/10.1016/j.jpowsour.2013.05.045.

38. Kulkarni, N.; Cho, J. I. S.; Jervis, R.; Roberts, E. P. L.; Francesco, I.; Kok, M. D. R.; Shearing, P. R.; Brett, D. J. L. The effect of non-uniform compression on the performance of polymer electrolyte fuel cells. *J. Power Sources* **2022**, *521*, 230973. DOI: 10.1016/j.jpowsour.2021.230973.

39. Chen, L.; Xu, Q.; Oener, S. Z.; Fabrizio, K.; Boettcher, S. W. Design principles for water dissociation catalysts in high-performance bipolar membranes. *Nat. Commun.* **2022**, *13* (1), 3846. DOI: 10.1038/s41467-022-31429-7 From NLM PubMed-not-MEDLINE.

40. Krivina, R. A.; Lindquist, G. A.; Yang, M. C.; Cook, A. K.; Hendon, C. H.; Motz, A. R.; Capuano, C.; Ayers, K. E.; Hutchison, J. E.; Boettcher, S. W. Three-electrode study of electrochemical ionomer degradation relevant to anion-exchange-membrane water electrolyzers. *ACS Appl. Mater. Interfaces* **2022**. DOI: 10.1021/acsami.1c22472.

41. Oener, S. Z.; Foster, M. J.; Boettcher, S. W. Accelerating water dissociation in bipolar membranes and for electrocatalysis. *Science* **2020**, *369*, 1099-1103.

42. Strathmann, H.; Krol, J. J.; Rapp, H.-J.; Eigenberger, G. Limiting current density and water dissociation in bipolar membranes. *J. Membr. Sci.* **1997**, *125*, 123-142.

43. Simons, R. Strong electric field effects on proton transfer between membrane-bound amines and water. *Nature* **1979**, *280*, 824-826.

44. Mafé, S.; Ramírez, P. Electrochemical characterization of polymer ion-exchange bipolar membranes. *Acta Polym.* **1997**, *48* (7), 234-250. DOI: https://doi.org/10.1002/actp.1997.010480702 (acccessed 2024/02/08).

45. Hurwitz, H. D.; Dibiani, R. Experimental and theoretical investigations of steady and transient states in systems of ion exchange bipolar membranes. *J. Membr. Sci.* **2004**, *228* (1), 17-43. DOI: https://doi.org/10.1016/j.memsci.2003.09.009.

46. Blommaert, M. A.; Aili, D.; Tufa, R. A.; Li, Q.; Smith, W. A.; Vermaas, D. A. Insights and challenges for applying bipolar membranes in advanced electrochemical energy systems. *ACS Energy Lett* **2021**, *6* (7), 2539-2548. DOI: 10.1021/acsenergylett.1c00618.

47. Simons, R.; Khanarian, G. Water dissociation in bipolar membranes Experiments and theory. *J. Membrane Biol.* **1978**, *38*, 11-30.

48. Lovrecek, B.; Kunst, B. Electrochemical Properties of the Ion-Exchange Membranes Junction. I. *Croat. Chem. Acta* **1962**, *34*.

49. Chen, Y.; Martínez, R. J.; Gervasio, D.; Baygents, J. C.; Farrell, J. Water splitting promoted by electronically conducting interlayer material in bipolar membranes. *J. Appl. Electrochem.* **2020**, *50* (1), 33-40. DOI: 10.1007/s10800-019-01365-4.

50. Chen, Y.; Wrubel, J. A.; Klein, W. E.; Kabir, S.; Smith, W. A.; Neyerlin, K. C.; Deutsch, T. G. High-performance bipolar membrane development for improved water dissociation. *ACS Applied Polymer Materials* **2020**, *2* (11), 4559-4569. DOI: 10.1021/acsapm.0c00653.

51. Huang, C.; Xu, T. Electrodialysis with bipolar membranes for sustainable development. *Environmental Science & Technology* **2006**, *40*, 5233-5243.

52. Strathmann, H. *Ion-exchange membrane separation processes*; Elsevier B.V., 2004.

53. Zhang, Z. B. Low-Temperature Electrochemical Cement Clinker Production. *ACS Energy Lett.* **2023**, *8* (9), 3927-3934. DOI: 10.1021/acsenergylett.3c01211.

54. Xu, Q.; Oener, S. Z.; Lindquist, G.; Jiang, H.; Li, C.; Boettcher, S. W. Integrated Reference Electrodes in Anion-Exchange-Membrane Electrolyzers: Impact of Stainless-Steel Gas-Diffusion Layers and Internal Mechanical Pressure. *ACS Energy Lett.* **2021**, *6* (2), 305-312. DOI: 10.1021/acsenergylett.0c02338.

55. Bender, G.; Carmo, M.; Smolinka, T.; Gago, A.; Danilovic, N.; Mueller, M.; Ganci, F.; Fallisch, A.; Lettenmeier, P.; Friedrich, K. A.; et al. Initial approaches in benchmarking and round robin testing for proton exchange membrane water electrolyzers. *Int. J. Hydrogen Energy* **2019**, *44* (18), 9174-9187. DOI: https://doi.org/10.1016/j.ijhydene.2019.02.074.

56. Stähler, M.; Stähler, A.; Scheepers, F.; Carmo, M.; Lehnert, W.; Stolten, D. Impact of porous transport layer compression on hydrogen permeation in PEM water electrolysis. *Int. J. Hydrogen Energy* **2020**, *45* (7), 4008-4014. DOI: https://doi.org/10.1016/j.ijhydene.2019.12.016.

57. Yun, S.-H.; Shin, S.-H.; Lee, J.-Y.; Seo, S.-J.; Oh, S.; Choi, Y.-W.; Moon, S. H. Effect of pressure on through-plane proton conductivity of polymer electrolyte membranes. *J. Membr. Sci.* **2012**, *417*, 210-216.

58. Kim, Y.; Walker, W. S.; Lawler, D. F. Electrodialysis with spacers: Effects of variation and correlation of boundary layer thickness. *Desalination* **2011**, *274* (1-3), 54-63. DOI: 10.1016/j.desal.2011.01.076.

59. Pourcelly, G. Electrodialysis with bipolar membranes Principles, optimization, and applications. *Journal of Electrochemistry* **2002**, *38* (8), 919-926.

60. Strathmann, H. Electrodialysis, a Mature Technology With a Multitude of New Applications. *Desalination* **2010**, *264* (3), 268-288. DOI: 10.1016/j.desal.2010.04.069.

61. Marin, D. H.; Perryman, J. T.; Hubert, M. A.; Lindquist, G. A.; Chen, L.; Aleman, A. M.; Kamat, G. A.; Niemann, V. A.; Stevens, M. B.; Regmi, Y. N.; et al. Hydrogen production with seawater-resilient bipolar membrane electrolyzers. *Joule* **2023**, *7* (4), 765-781. DOI: https://doi.org/10.1016/j.joule.2023.03.005.

62. Vermaas, D. A.; Wiegman, S.; Nagaki, T.; Smith, W. A. Ion transport mechanisms in bipolar membranes for (photo)electrochemical water splitting. *Sustain. Energy Fuels* **2018**, *2* (9), 2006-2015, 10.1039/C8SE00118A. DOI: 10.1039/C8SE00118A.

63. Toh, W. L.; Dinh, H. Q.; Chu, A. T.; Sauvé, E. R.; Surendranath, Y. The role of ionic blockades in controlling the efficiency of energy recovery in forward bias bipolar membranes. *Nat. Energy* **2023**, *8* (12), 1405-1416. DOI: 10.1038/s41560-023-01404-7.

64. Chen, L.; Xu, Q.; Boettcher, S. W. Kinetics and mechanism of heterogeneous voltage-driven water-dissociation catalysis. *Joule* **2023**, *7* (8), 1867-1886. DOI: https://doi.org/10.1016/j.joule.2023.06.011.

65. Lucas, É.; Han, L.; Sullivan, I.; Atwater, H. A.; Xiang, C. Measurement of ion transport properties in ion exchange membranes for photoelectrochemical water splitting. *Front. Energy Res.* **2022**, *10*. DOI: 10.3389/fenrg.2022.1001684.

66. Parnamae, R.; Tedesco, M.; Wu, M. C.; Hou, C. H.; Hamelers, H. V. M.; Patel, S. K.; Elimelech, M.; Biesheuvel, P. M.; Porada, S. Origin of limiting and overlimiting currents in bipolar membranes. *Environ. Sci. Technol.* **2023**, *57* (26), 9664-9674. DOI: 10.1021/acs.est.2c09410.

67. Newman, J.; Bennion, D.; Tobias, C. W. Mass transfer in concentrated binary electrolytes. *Ber. Bunsen-Ges. Phys. Chem.* **1965**, *69* (7), 608-612. DOI: https://doi.org/10.1002/bbpc.19650690712.

68. Slade, S.; Campbell, S. A.; Ralph, T. R.; Walsh, F. C. Ionic conductivity of an extruded nafion 1100 EW series of membranes. *J. Electrochem. Soc.* **2002**, *149* (12), A1556. DOI: 10.1149/1.1517281.

69. Liu, L.; Chen, W.; Li, Y. An overview of the proton conductivity of nafion membranes through a statistical analysis. *J. Membr. Sci.* **2016**, *504*, 1-9. DOI: 10.1016/j.memsci.2015.12.065.

70. Fernandes, A. C.; Ticianelli, E. A. A performance and degradation study of Nafion 212 membrane for proton exchange membrane fuel cells. *J. Power Sources* **2009**, *193* (2), 547-554. DOI: https://doi.org/10.1016/j.jpowsour.2009.04.038.

71. Khalid, H.; Najibah, M.; Park, H. S.; Bae, C.; Henkensmeier, D. Properties of anion exchange membranes with a focus on water electrolysis. In *Membranes*, 2022; Vol. 12.

72. Mauritz, K. A.; Moore, R. B. State of understanding of Nafion. *Chem. Rev.* **2004**, *104* (10), 4535–4585.

73. Kusoglu, A.; Weber, A. Z. New Insights into Perfluorinated Sulfonic-Acid Ionomers. *Chem Rev* **2017**, *117* (3), 987-1104. DOI: 10.1021/acs.chemrev.6b00159 From NLM PubMed-not-MEDLINE.

74. Vinodh, R.; Kalanur, S. S.; Natarajan, S. K.; Pollet, B. G. Recent Advancements of Polymeric Membranes in Anion Exchange Membrane Water Electrolyzer (AEMWE): A Critical Review. In *Polymers*, 2023; Vol. 15.

75. Ahmad, M.; Ahmed, M. Characterization and applications of ion-exchange membranes and selective ion transport through them: a review. *J. Appl. Electrochem.* **2023**, *53* (8), 1537-1562. DOI: 10.1007/s10800-023-01882-3.

76. IEA. *Global energy and climate model*; Paris, 2023. https://www.iea.org/reports/global-energy-and-climate-model.

77. Oener, S. Z.; Twight, L. P.; Lindquist, G. A.; Boettcher, S. W. Thin cation-exchange layers enable high-current-density bipolar membrane electrolyzers via improved water transport. *ACS Energy Lett.* **2021**, *6* (1), 1-8. DOI: 10.1021/acsenergylett.0c02078.

78. Shen, C.; Wycisk, R.; Pintauro, P. N. High performance electrospun bipolar membrane with a 3D junction. *Energy & Environmental Science* **2017**, *10* (6), 1435-1442. DOI: 10.1039/c7ee00345e.

79. Stokke, D. D.; Wu, Q.; Han, G. Fundamentals of Adhesion. In *Introduction to wood and natural fiber composites.*, 1 ed.; John Wiley & Sons, Incorporated, 2013; pp 129-168.

80. Bradley, L. C.; Bade, N. D.; Mariani, L. M.; Turner, K. T.; Lee, D.; Stebe, K. J. Rough Adhesive Hydrogels (RAd gels) for Underwater Adhesion. *ACS Appl Mater Inter* **2017**, *9* (33), 27409-27413. DOI: 10.1021/acsami.7b08916 From NLM PubMed-not-MEDLINE.

81. Nemati, M.; Hosseini, S. M.; Shabanian, M. Developing thin film heterogeneous ion exchange membrane modified by 2-acrylamido-2-methylpropanesulfonic acid hydrogel-co-super activated carbon nanoparticles coating layer. *Korean J. Chem. Eng.* **2017**, *34* (6), 1813-1821.

82. Clemens, A. L.; Jayathilake, B. S.; Karnes, J. J.; Schwartz, J. J.; Baker, S. E.; Duoss, E. B.; Oakdale, J. S. Tuning Alkaline Anion Exchange Membranes through Crosslinking: A Review of Synthetic Strategies and Property Relationships. *Polymers* **2023**, *15* (6), 1534.

83. Guo, M.; Ban, T.; Wang, Y.; Wang, X.; Zhu, X. "Thiol-ene" crosslinked polybenzimidazoles anion exchange membrane with enhanced performance and durability. *J. Colloid Interface Sci.* **2023**, *638*, 349-362. DOI: https://doi.org/10.1016/j.jcis.2023.01.137.

84. Yan, N.; Paul, D. R.; Freeman, B. D. Water and ion sorption in a series of cross-linked AMPS/PEGDA hydrogel membranes. *Polymer* **2018**, *146*, 196-208. DOI: 10.1016/j.polymer.2018.05.021.

85. Zhan, K.; Kim, C.; Sung, K.; Ejima, H.; Yoshie, N. Tunicate-Inspired Gallol Polymers for Underwater Adhesive: A Comparative Study of Catechol and Gallol. *Biomacromolecules* **2017**, *18* (9), 2959-2966. DOI: 10.1021/acs.biomac.7b00921 From NLM Medline.

86. Suneetha, M.; Rao, K. M.; Han, S. S. Mussel-Inspired Cell/Tissue-Adhesive, Hemostatic Hydrogels for Tissue Engineering Applications. *ACS Omega* **2019**, *4* (7), 12647-12656. DOI: 10.1021/acsomega.9b01302.

87. Hou, Y.; Jiang, N.; Sun, D.; Wang, Y.; Chen, X.; Zhu, S.; Zhang, L. A fast UV-curable PU-PAAm hydrogel with mechanical flexibility and self-adhesion for wound healing. *RSC Adv* **2020**, *10* (9), 4907-4915. DOI: 10.1039/c9ra10666a From NLM PubMed-not-MEDLINE.

88. Qu, K.; Yuan, Z.; Wang, Y.; Song, Z.; Gong, X.; Zhao, Y.; Mu, Q.; Zhan, Q.; Xu, W.; Wang, L. Structures, properties, and applications of zwitterionic polymers. *ChemPhysMater* **2022**, *1* (4), 294-309. DOI: 10.1016/j.chphma.2022.04.003.

89. McDonald, M. B.; Freund, M. S. Graphene oxide as a water dissociation catalyst in the bipolar membrane interfacial layer. *ACS Appl Mater Inter* **2014**, *6* (16), 13790-13797. DOI: 10.1021/am503242v From NLM PubMed-not-MEDLINE.

90. Lucas, É.; Bui, J. C.; Hwang, M.; Wang, K.; Bell, A. T.; Weber, A. Z.; Ardo, S.; Atwater, H. A.; Xiang, C. Asymmetric bipolar membrane for high current density electrodialysis operation with exceptional stability. *ChemRxiv* **2023**.

91. Yamate, T.; Fujiwara, T.; Yamaguchi, T.; Suzuki, H.; Akazome, M. Exploiting CH/π interactions in robust supramolecular adhesives. *Polymer Chemistry* **2018**, *9* (32), 4303-4308, 10.1039/C8PY00592C. DOI: 10.1039/C8PY00592C.

92. Bjork, J.; Hanke, F.; Palma, C.-A.; Samori, P.; Cecchini, M.; Persson, M. Adsorption of Aromatic and Anti-Aromatic Systems on Graphene through π-π Stacking. *J. Phys. Chem. Lett* **2010**, *1*, 3407-3412. DOI: 10.1021/jz101360k.

93. Grimme, S. Do special noncovalent π-π stacking interactions really exist? *Angewandte Chemie - International Edition* **2008**, *47*, 3430-3434. DOI: 10.1002/anie.200705157.

94. Wheeler, S. E. Understanding Substituent Effects in Noncovalent Interactions Involving Aromatic Rings. *Acc. Chem. Res.* **2013**, *46* (4), 1029-1038. DOI: 10.1021/ar300109n.

95. Ma, J. C.; Dougherty, D. A. The Cation−π Interaction. *Chem. Rev.* **1997**, *97*, 1303-1324.

96. Ruan, H.; Zheng, Z.; Pan, J.; Gao, C.; Van der Bruggen, B.; Shen, J. Mussel-inspired sulfonated polydopamine coating on anion exchange membrane for improving permselectivity and anti-fouling property. *J. Membr. Sci.* **2018**, *550*, 427-435. DOI: 10.1016/j.memsci.2018.01.005.

97. Hossen, M. J.; Sarkar, S. D.; Uddin, M. M.; Roy, C. K.; Azam, M. S. Mussel-Inspired Adhesive Nano-Filler for Strengthening Polyacrylamide Hydrogel. *ChemistrySelect* **2020**, *5* (29), 8906-8914. DOI: 10.1002/slct.202001632.

98. McCloskey, B. D.; Park, H. B.; Ju, H.; Rowe, B. W.; Miller, D. J.; Chun, B. J.; Kin, K.; Freeman, B. D. Influence of polydopamine deposition conditions on pure water flux and foulant adhesion resistance of reverse osmosis, ultrafiltration, and microfiltration membranes. *Polymer* **2010**, *51* (15), 3472-3485. DOI: 10.1016/j.polymer.2010.05.008.

99. Kim, S.; Jang, L. K.; Park, H. S.; Lee, J. Y. Electrochemical deposition of conductive and adhesive polypyrrole-dopamine films. In *Scientific reports*, 2016; Vol. 6, p 30475.

100. Pham, M.-H.; Barz, D. P. J. Bonding Nafion ® with Polydimethysiloxane A Versatile Approach towards Ion-exchange Membrane Microfluidic Devices. *J. Membr. Sci.* **2017**, *537*, 310-314.

101. Matinlinna, J. P.; Lassila, L. V.; Dahl, J. E. Promotion of Adhesion Between Resin and Silica-coated Titanium by Silane Monomers and Formic Acid Catalyst. *Silicon* **2010**, *2* (2), 87-93. DOI: 10.1007/s12633-010-9041-z.

102. Li, Q.; Wang, L.; Liu, Q.; Hong, W.; Yang, C. Fatigue Damage-Resistant Physical Hydrogel Adhesion. *Front Robot AI* **2021**, *8*, 666343. DOI: 10.3389/frobt.2021.666343 From NLM PubMed-not-MEDLINE.

103. Szentirmay, M. N.; Campbell, L. F.; Martin, C. R. Silane Coupling Agents for Attaching Nafion to Glass and Silica. *Anal. Chem.* **1986**, *58*, 661-662. DOI: 10.1021/ac00294a042,.

104. Mueller, H.; Puetter, H. Production of bipolar membranes. United States 4670125, 1987.

105. Umemura, K.; Naganuma, T.; Miyake, H. Bipolar membrane. Europe 1993.

106. Lee, L. T. C.; Dege, G. J.; Liu, K.-J. High performance, quality controlled bipolar membrane. United States 4,057,481, 1977.

107. Vandiver, M. A.; Caire, B. R.; Pandey, T. P.; Li, Y.; Seifert, S.; Kusoglu, A.; Knauss, D. M.; Herring, A. M.; Liberatore, M. W. Effect of hydration on the mechanical properties and ion conduction in a polyethylene-b-poly(vinylbenzyl trimethylammonium) anion exchange membrane. *Journal of membrane science.* **2016**, *497*, 67-76. DOI: 10.1016/j.memsci.2015.09.034.

108. Allushi, A.; Pham, T. H.; Jannasch, P. Highly conductive hydroxide exchange membranes containing fluorene-units tethered with dual pairs of quaternary piperidinium cations. *J. Membr. Sci.* **2021**, *632*, 119376. DOI: https://doi.org/10.1016/j.memsci.2021.119376.

109. Wang, L.; Rojas-Carbonell, S.; Hu, K.; Setzler, B. P.; Motz, A. R.; Ueckermann, M. E.; Yan, Y. Standard Operating Protocol for Ion-Exchange Capacity of Anion Exchange Membranes. *Front. Energy Res.* **2022**, *10*, Methods. DOI: 10.3389/fenrg.2022.887893.

110. Tejuosho, T.; Kollipara, S.; Patankar, S.; Sampath, J. Dynamics of Polymer Chains in Disperse Melts: Insights from Coarse-Grained Molecular Dynamics Simulations. *J. Phys. Chem. B* **2024**, *128* (47), 11846-11854. DOI: 10.1021/acs.jpcb.4c05610.